Binder Film Thickness Effect on Aggregate Contact Behavior

Dong Wang

Thesis submitted to the faculty of

Virginia Polytechnic Institute and State University

in partial fulfillment of the requirements for the degree of

Master of Science

In

Civil Engineering

Linbing Wang, Chair
Gerardo W. Flintsch
Marte S. Gutierrez

August 2, 2007

Blacksburg, Virginia

Keywords: Contact Model, X-Ray Tomography, Composite Material, Binder Film

Binder Film Thickness Effect on Aggregate Contact Behavior

Dong Wang

(ABSTRACT)

This study presents a study on the binder film thickness effect on aggregate contact behavior. As a three-phase material composed of aggregates, asphalt binder and air voids, asphalt mixture could be considered as a visco-elastic material in the low stress level. Since the behavior of the mixture depends largely on the relationship of different components, a well developed contact model for micro-structural modeling is very important for understanding the deformation mechanism of the mixture. In this study, the contact modeling of asphalt mixture was reviewed and the numerical tools used to investigate the micromechanical behavior of asphalt mixture will also be introduced. By using the cabinet x-ray tomography system, the displacement and resistant force of a system of particles bonded by a thin layer binder are measured and recorded. Then, the results are compared with the theoretical solutions of a normal compliance model for a system comprised of two elastic particles bonded by a thin layer of visco-elastic binder. A closed-form time-dependent relationship between the contact forces and the relative particle/binder movements was developed. A reasonable agreement between experiments results and model predicted results is obtained combined with parametric analysis.

This thesis is dedicated to my parents Xiaomin Wang and Xiaoming Wan

ACKNOWLEDGEMENT

The author wants to thank his advisor, Dr. Linbing Wang for his support and patient supervision. His valuable and constructive advice and comments are greatly appreciated.

The author also wants to thank his advisory committee members, Dr. Gerardo W. Flintsch, and Dr. Marte S. Gutierrez, for their valuable advices and support during coursework and thesis preparation.

The author would like to thank his colleagues and friends for their help both in and out of office and laboratory.

The research was made possible with the support from the Department of Civil and Environmental Engineering and VTTI of Virginia Tech.

CONTENT

LIST OF FIGURES

LIST OF TABLES

Chapter 1. Introduction

1.1. Background

Asphalt mixture is a composite material which consists of interspersed aggregates, asphalt binder and air voids. The constitutive behavior of the material depends largely on the interaction between the aggregates and asphalt binder. The aggregate skeleton determines the load carrying mechanism and the asphalt binder serves as an adherent which enables the mix to hold tensile and shear stresses. A comprehensive understanding of the mechanical behavior of aggregate-binder system is critical for research in the area of the deformation mechanism of asphalt mixtures. To study the constitutive behavior of an aggregate-binder system, the contact between aggregates coated with asphalt binder is the key problem to solve. A contact model which properly shows the relationship between the contact force and relative movement is needed. Combined with the mechanical model, numerical tools could be incorporated into the study, such as the Finite Element Method (FEM) and Discrete Element Method (DEM). Both of the FEM and the DEM are utilized in the simulation of mechanical materials. The former is based on the continuum approach and has been successful in capturing the stress-strain distribution within the asphalt mixtures and its effect on the stiffness anisotropy. The latter based on the discrete approach could analyze the individual characteristic effects of each component in the mixture, such as the influence of shape, gradation and relative slippage of aggregates. The proper representation of the asphalt mixture internal structure is possible through the use of image analysis techniques. These techniques are utilized to accurately capture the actual microstructure of the asphalt mixture. Such images offer a realistic representation of the internal structure of asphalt mixtures and could be used to analyze the deformation of the composite material. Given the proper internal structure and constitutive contact models, the simulation could avoid

huge amount of sample preparation work in the lab and provide reliable results in the research of the asphalt mixtures.

1.2. Research Objectives

Three major objectives are identified for this work:

1- Study the visco-elatic behavior of the asphalt mixture. Review the contact model used to characterize the behavior of the asphalt mixture. Review the numerical tools used in the research of asphalt mixtures including both the simulation methods and the image analysis system.

2- Introduce the normal compliance model for a visco-elastic binder layer contact problem developed by Han Zhu at al (1996(b)) in details.

3- Develop the lab test with the use of a cabinet x-ray microscopy system to validate the contact model.

1.3. Research tasks and organization

This thesis is organized into five chapters. Chapter 2 presents the literature review of subjects related to this study. The main part of this task focuses on the visco-elastic behavior of asphalt mixture and the simulation techniques used to model the deformational behavior of asphalt mixture. Chapter 3 introduces the normal compliance model which consists of two elastic particles coated with a visco-elastic asphalt binder layer. The lab test used to validate the model is also described. Chapter 4 provides the test results and compares the test results with the theoretical solutions. Chapter 5 concludes the analysis of the test results and gives some recommendations for further study

Chapter 2. Literature Review

2.1. Introduction

This chapter starts with the review of concept of visco-elastic material which is currently being used to characterize the rheological behavior of asphalt binder and mixture. The superpave tests of the behavior of asphatic binder and the mixture are introduced. It documents the contact models developed to describe the micro-mechanical behavior of the mixture and the numerical tools used to investigate the material.

2.2. Visco-elastic Behavior of Asphalt Mixture

2.2.1. Visco-elastic material

The response of materials to load is defined by the stress-strain behavior. Elastic material shows time-independent behavior and can be characterized by its elastic modulus. Viscous material behaves time-dependently and exhibits constant non-zero strain after the stress is removed. Asphalt binder exhibits both elastic and viscous behaviors; hence it is considered visco-elastic materials. Figure 2.1 shows the stress-strain result of the three materials under a simple creep test. A constant load is applied to a material at time t_0 and removed at time t_1 (Figure 2.1).

The elastic material immediately deforms to a constant strain after a load is applied and recovers to zero when the loading is removed (Figure 2-1a). A linear viscous material deforms at a constant rate when the load is applied at time t_0 and continues to deform at the same rate until the load is removed, beyond which there is no further strain change (Figure 2.1b). Visco-elastic materials experience an immediate strain followed by a gradual time-dependent strain increase up to time t_1. When the load is removed the material experiences a partial immediate strain recovery, followed by a time-dependent

strain recovery (Figure 2.1c). The amount of recoverable strain is a function of the time allowed for recovery, while the non-recoverable strain is referred to as permanent deformation. Most viscoelastic materials exhibit a significant amount of delayed elastic response that is time-dependent but completely recoverable. Some binders exhibit significant plastic strains over finite recovery times, hence exhibiting a viscoplastic behavior.

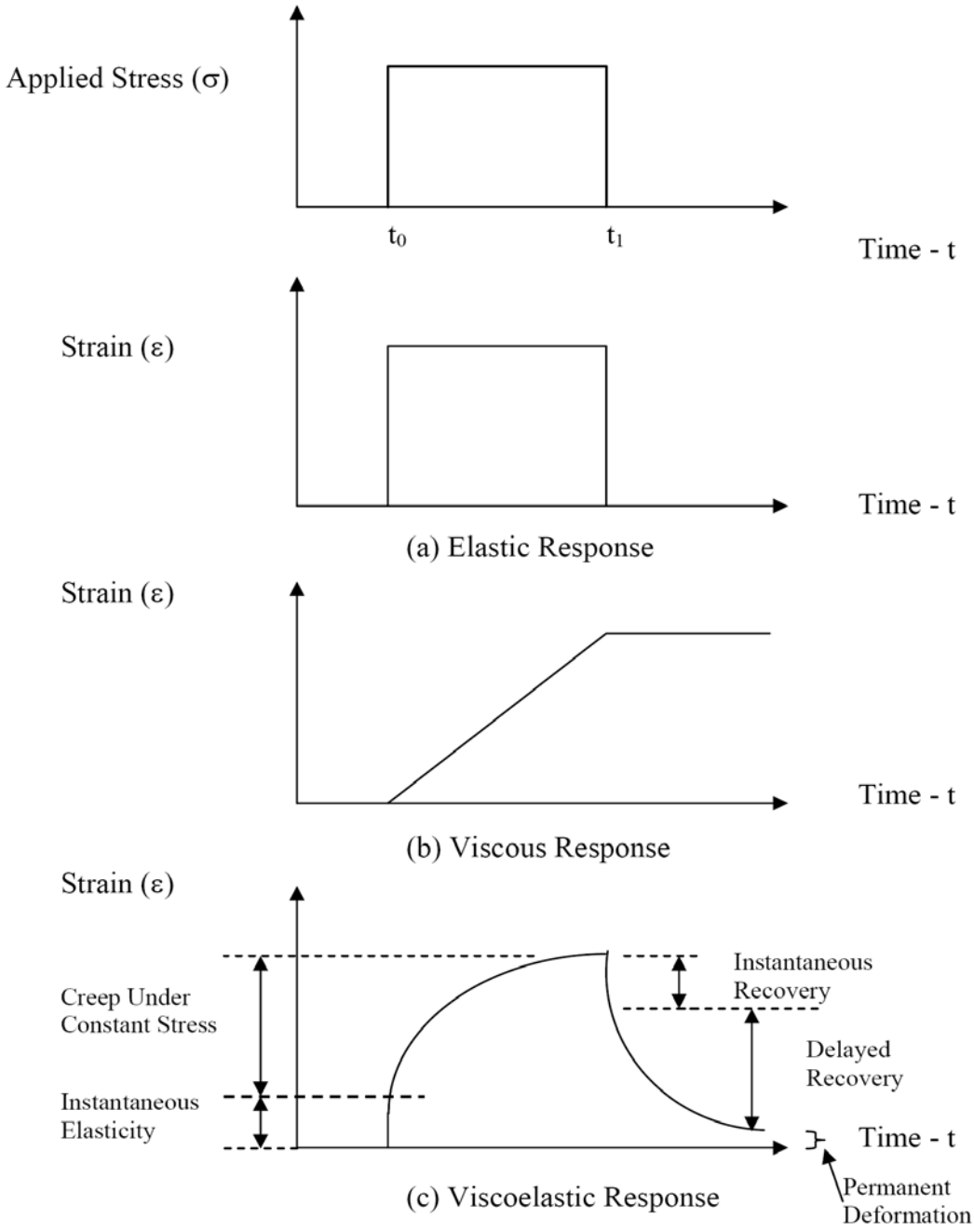

Figure 2-1 Idealized Response of Elastic, Viscous, and Viscoelastic Materials under Constant Stress Loading (a) Elastic material (b) Viscous Material (c) Visco-elastic material (A.Abbas 2004)

2.2.2. Dynamic Shear Rheometer Test of Asphalt Binder

The dynamic shear rheometer (DSR) (Figure 2-2), is used to characterize the viscous and elastic behavior of asphalt binders at high and intermediate temperature. In

this study we will use some DSR tests results achieved by other researchers in the model study. The range of complex shear modulus and phase angle of the binder we used in the test will be obtained from the literature review. Details will be discussed in the chapter 4.

The DSR measures the complex shear modulus G^* and phase angle δ of the binder at the desired temperature and frequency of loading. Complex modulus G^* can be considered as the total resistance of the binder to deformation when repeatedly sheared. As shown in the Figure 2-3, the complex modulus consists of two components: storage modulus G' or the elastic part, and loss modulus G'' or the viscous part. The phase angle represents the immediate elastic and the delayed viscous responses of the binder obtained from the lag between the measured shear stresses and the induced strains in a strain-controlled device (Figure 2-4). For elastic materials the phase angle value is zero, whereas for purely viscous materials, the phase angle is 90^o. Thus, the phase angle is important in describing the visco-elastic properties of a material such as asphalt. Materials with higher storage moduli have greater ability to recover from deformation, and materials with higher loss moduli have greater ability to resist deformation at any prescribed frequency.

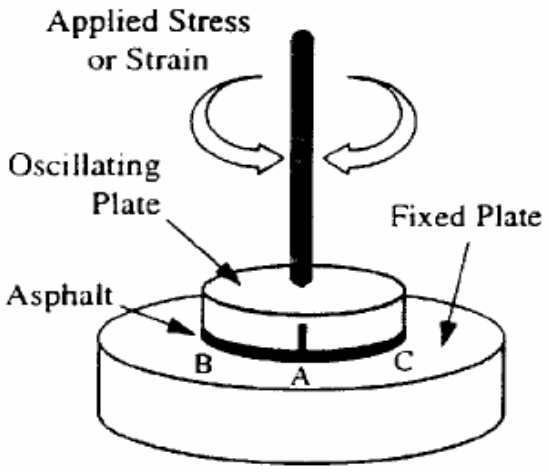

Figure 2-2 Dynamic Shear Rheometer (DSR) (A.Abbas 2004).

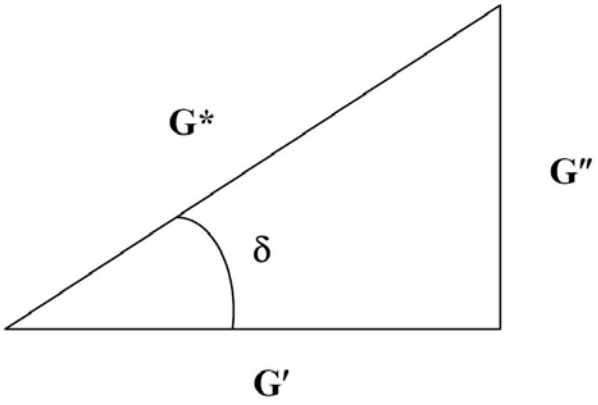

Figure 2-3 Relationship among Complex Shear Modulus (G*), Storage Modulus (G′), Loss Modulus (G″), and Loss Tangent tan(δ)

$$G^*(\omega) = \sqrt{G'(\omega)^2 + G''(\omega)^2} \quad \textbf{(2-1)}$$

$$G'(\omega) = G^*(\omega)\cos(\delta(\omega)) \quad \textbf{(2-2)}$$

$$G''(\omega) = G^*(\omega)\sin(\delta(\omega)) \quad \textbf{(2-3)}$$

$$\delta = \tan^{-1}\frac{G''(\omega)}{G'(\omega)} \quad \textbf{(2-4)}$$

where,

G*(ω) = complex shear modulus at frequency ω,

G′(ω) = dynamic storage modulus at frequency ω,

G″(ω) = dynamic loss modulus at frequency ω,

δ(ω) = phase angle at frequency ω, and

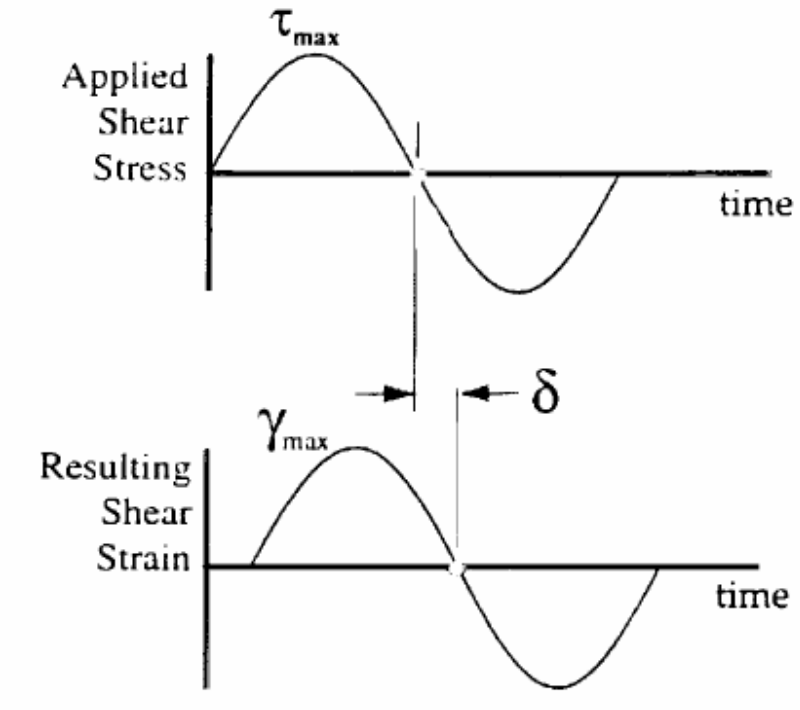

Figure 2-4 Stress-Strain Response of a Viscoelastic Material (A.Abbas 2004).

The DSR testing procedure is given in AASHTO TP5. As shown in the Figure2-2, the asphalt binder sample is constrained between a fixed plate and an oscillating plate. The thickness of the asphalt binder depends on the testing temperature. High test temperatures require a small gap of 1mm. While 2-mm gaps are used for lower temperatures. Also, two spindle diameters are used; large spindle (25mm) for high temperatures and small spindle (8mm) for low test temperatures. All Superpave DSR test are conducted at a frequency of 10 radians per second, which is equivalent to 1.59Hz. The software uses Equation (2-5) to calculate G*, and the following formulas to calculate the maximum shear stress, τ_{max}, and the maximum shear strain, γ_{max},

$$G^*(\omega) = \frac{\tau_{max}}{\gamma_{max}} \quad \textbf{(2-5)}$$

Where,

G*(ω)= dynamic shear modulus at frequency ω,

τ_{max} = amplitude of the sinusoidal shear stress, and

γ_{max} = amplitude of the sinusoidal shear strain.

$$\tau_{max} = \frac{2T}{\pi r^3} \quad \textbf{(2-1)}$$

$$\gamma_{max} = \frac{\theta r}{h} \quad \textbf{(2-2)}$$

Where,

T = maximum applied torque

r = radius of binder specimen (either 12.5mm or 4mm)

θ = rotation angle

h = specimen height (either 1mm or 2mm).

2.3. Contact model

Asphalt mixture can be considered to be three phase composites consisting of asphalt, aggregates and air voids. Because of the complex heterogeneous nature of the material, the macro load carrying behavior depends on many micro-phenomena that occur at the aggregate/binder level. Some important micro behaviors are related to binder properties including volume percentage, elastic moduli, time-dependent response, aging hardening, microcracking, and debonding from aggregates. Other microstructural features include aggregate size, shape, texture and packing geometry. Because of these issues it appears that a micromechanical model would be best suited to properly simulate such a material. Furthermore, micromechanics offer the possibility to more accurately predict asphalt performance and to relate such behavior to particular mix parameters such as binder properties, aggregate gradation, and sample compaction.

Van der Poel (1958) attempted to model the behavior of asphalt mixture by calculating the rigidity of a concentrated solution of elastic spheres in an elastic medium, using a method developed for dilute dispersions by Frohlich and Sack. The model was

reported to give reasonable agreement with experimental measurements of dynamic mix stiffness up to a volume fraction of 60 % aggregate.

Hills (1973) attempted to develop theoretical models for the long time creep behavior of asphalt mixes. His modeling approach described the internal structure in terms of a characteristic asphalt thickness, and the evolution of this state variable as a function of the macroscopic straining of the material. The macroscopic strain of a mix was assumed to be accommodated, on a microscopic scale, by displacements of adjacent aggregate particles in both shear and compression. These displacements were assumed to be independent of each other. It was further postulated that the macroscopic strain of the mix was uniquely related to the shear displacements of adjacent aggregate particles. The microscopic shear resistance of the asphalt was considered to be controlled by the thickness of the asphalt. The effect of compression was taken into account by changing the thickness of the asphalt. The asphalt was modeled as an incompressible, linear viscous fluid. The general forms of the constitutive equations were given in terms of the 'stiffness' of asphalt, S_{bit}, in the region $S_{bit} < 5$ MPa. Hills' model was based on an empirical estimation of the evolution of film thickness under deformation rather than by analysis of the deformation of the film. The model depended on curve fitting to experimental data to obtain numerical data.

Cheuang at al (1997) used the isolated model for micromechanical modeling of the stage I sintering process, when the dominant mechanism of contact deformation is rate-independent plasticity or power law creep. A compatible strain rate field is assumed for describing the motion of individual particles. The constraints on the motion of each contact are determined by analysis of the corresponding deformation mechanism. Using kinematics bounds, the macroscopic deformation behavior can then be estimated by integrating the microscopic deformation behavior, assuming that individual contacts deform in isolation. They assumed that all of the aggregate particles are separated by thin films of asphalt; the constraints on the relative motion of the particles will largely be determined by the deformation behavior of the bitumen films until they become so thin that their stiffness becomes comparable with the stiffness of the aggregate particles. They also assumed that asphalt existing in larger quantities of particles within the random aggregate skeleton will have only secondary effects on the deformation behavior of the

mix. The assumption of isolated contacts means asphalt displaced by the deformation of each contact flows into an air void rather than into an adjacent contact. It is therefore necessary for the volume of asphalt displaced to be small compared with the volume of voids. Analysis based on the assumption of isolated contact behavior provides a theoretical limiting case solution regarding the macroscopic behavior of the idealized mix, corresponding to the case when microscopic deformation occurs at all distributed thin film bitumen contacts.

Uddin (1998) presented a micromechanical analysis method for calculating the creep compliance of asphaltic mixes on a microscopic level using laboratory viscoelastic characterization of the binder and elastic material properties of the aggregates at a given temperature. The micromechanical model is based upon the "method of cells" (MOC) developed to predict viscoelastic response of resin matrix composites. The properties of the aggregate are assumed to be linear elastic and can be described by the elastic constitutive relationship. A time-stepping algorithm was developed for a viscoelastic material with a Prony series representation of the time-dependent properties. And the micromechanical model was incorporated in a microcomputer program which calculates the viscoelastic response of the mix and predicts the mix stiffness. It is reported that reasonably good agreement is found between the predicted modulus and measured modulus of the mix if proper percent air voids are considered in the micromechanical model.

Zhong and Chang (1999) applied a micromechanics approach to investigate the interparticle behavior of two particles connected by a binder. The model is based on the premises that the interparticle binder initially contains microcracks. As a result of external loading, these microcracks propagate and grow. Thus, binders are weakened and fail. Theory of fracture mechanics was employed to model the propagation and growth of the microcracks. The contact law is then incorporated in the analysis for the overall damage behavior of material using a discrete element method. Using this model, the stress-strain behaviors under uniaxial and biaxial conditions were simulated. And it is reported that a reasonable agreement is found between the predictions and experimental results.

Levenberg and Uzan (2003) developed a triaxial cross-anisotropic viscoelastic-viscoplastic constitutive model for asphalt aggregate mixtures for the small-strain domain. The model follows the concept of strain decomposition by separately analyzing the viscoelastic and viscoplastic strain components. In order to calibrate the model, advanced triaxial testing was employed which included both hydrostatic and uniaxial creep and recovery cycles. The test-data is presented and analyzed along with the derivation of all model parameters. It is reported that the proposed model correlates extremely well with the entire test-data in both axial and radial directions.

Mazzotti and Savoia (2003) proposed an isotropic model for creep damage of concrete under uniaxial compression, where the combined effect of nonlinear viscous strain evolution and crack nucleation and propagation at high stress levels is considered. Strain splitting assumption is used for creep and damage contributions. Creep is modeled by a modified version of solidification theory. In the modeling of damage of concrete, a damage index based on positive strains is introduced. In particular cases, the proposed model reduces to linear viscoelasticity for long time low stress levels whereas, for very high stresses, tertiary creep causing failure at a finite time can be described. The effect of strength variation with time is also included. The model is numerically implemented to perform time integration of nonlinear equations by means of a modified version of exponential algorithm. The model was validated through comparison with experimental results and numerical examples are also presented, where the roles of concrete ageing and strength variation with time are investigated.

Huang et al (2004) presented a temperature dependent viscoplastic model that incorporated temperature and loading rate into the Hierarchical Single Surface plasticity based model. The model was able to reflect the nonlinear plasticity, as well as the temperature and loading rate dependencies of the asphalt mixtures. Triaxial compression, triaxial extension, and axial creep tests at three temperatures 28, 40 and 60°C were performed to calibrate the material properties. And they proposed an algorithm to compare the numerical analysis obtained from the model and experimental results. It is reported a reasonable agreement was observed from the back calculation and the experimental results.

Chehab and Kim (2005) reported a viscoelastoplastic continuum damage (VEPCD) model which is developed and validated under the auspices of the National Cooperative Highway Research Program 9-19 project, entitled "Advanced Mixture Characterization for Superpave Support and Performance Models Management." The VEPCD model was able to characterize the viscoelastic and viscoplastic responses of asphalt concrete in addition to microcracking. They validated the model under thermal loading conditions that are distinctively different from the mechanical loading conditions used in model development and calibration. Measured responses and fracture parameters from thermal strain restrained specimen tensile strength tests were conducted to compare with those predicted using the VEPCD model, the viscoelastic continuum damage model, and the linear viscoelastic model. It is reported that the ability of the VEPCD model to accurately characterize the tensile behavior of asphalt concrete under thermally induced loading was confirmed.

2.4. Numerical Methods

Sepehr et al. (1994) conducted a finite element analysis of a pavement structure with the asphalt layer represented by an idealized microstructure. Air voids were simulated by imposing small stiffness values to some of the elements. This analysis revealed significant information about the influence of the micro-structural properties on the macroscopic behavior of the pavement. It was observed that increasing the air voids from 1% to 5% resulted in 1.2% increase in pavement surface deflection. It was also shown that reducing the asphalt binder stiffness from 1000MPa to 250MPa resulted in 2.25% increase in the deflection. The influence of aggregate shape on pavement behavior was also investigated and 2% decrease in surface deflection was reported when round-shaped aggregates were replaced by aggregates of sharp edges.

Bahia et al. (1999) conducted finite element analyses using an idealized internal structure of asphalt mixture, whereby aggregates were represented by circular objects. Binder and aggregate elements were considered linear elastic materials. The objective of this analysis was to evaluate the deformation and strain distribution in asphalt mixes and its relation to the nonlinear mix behavior. It was observed that when applying 1% strain, the binder shear strain could be as high as 46%. Therefore, they suggested that within an

actual mixture, a wider range of film thickness would exist and a wider range of strain magnitude could be realized within the binder domain.

Abbas et al. (2004) incorporated a nonlinear viscoelastic material model in a FEM to analyze the asphalt concrete microstructure. The viscoelastic behavior of the asphalt mastic was defined using a mechanistic model, which was numerically solved using a convolution integral approach. To account for the asphalt binder non-linearity, the mechanical parameters were updated during the analysis according to the strain level within each element. The analysis was also used to analytically study some of the discrepancies observed between laboratory measurements of the asphalt mixture E* and G*.

Saadeh et al. (2003) extended the comparison between E* and G* to include both experimental and numerical measurements. They studied the main factors causing discrepancies between the axial and shear tests, which include the type of loading (stress versus strain-controlled), direction and reversal of principal stresses, and stress and strain distribution within the specimen. Using finite element simulations of these tests, they reported a Poisson's ratio between 1.0 and 1.5, depending on the test frequency, which is relatively smaller than that obtained experimentally. Therefore, they concluded that the FEM only captures the effect of the stress and strain distribution and does not capture the effect of the rest of these factors. It should be noted that the finite element analyses they considered included linear viscoelastic mastics and elastic aggregates.

Rothenburg et al. (1992) presented a micromechanical model of asphalt mixture based on discrete element techniques, whereby aggregates were modeled as polygons and the inter-particle forces were described using a mechanistic viscoelastic model. The objective of this work was to relate the asphalt mixture internal structure to its deformation characteristics. Particles were considered as plane elements that interact by means of contact forces. Simulation of angular aggregate particles with an arbitrary gradation was described by a particle generation algorithm. It was found that the complex performance of the granular matrix is the main reason for the nonlinear trends in mechanical response of asphalt mixture, and to a large degree its susceptibility to rutting in field situations. Simulations indicated that mix strength increased with the increase in the fraction of contacts and that at least 30% of contacts should be bound to get nonzero

strength. At least 20% of the contacts must be nonzero friction to develop shear resistance.

Chang and Meegoda (1997) used the DEM to describe different types of aggregate-aggregate and asphalt-aggregate contacts. They utilized mechanistic models to simulate the viscoelastic behavior of asphalt binder. They incorporated the Mohr-Coulomb failure criterion to account for the sliding of asphalt-coated particles due to rotation. Both macroscopic and microscopic behaviors were monitored during simulation. It was reported that the stress-strain behavior was properly captured even in the post-peak region.

Buttlar and You (2001) used DEM to simulate the behavior of asphalt mixture in the indirect tension test (IDT). They described the internal structure using clusters of circular particles. A linear contact model along with a bonding and sliding capabilities was used to define the particles' interaction. Their observations pointed out the significant contribution of aggregate interaction in accurately simulating the stiffness of asphalt mixtures, and hence, suggested the need for utilizing realistic aggregate shapes in microstructure models.

Given the proper mechanical contact model, the numerical simulation could avoid huge amount of sample preparation work in the lab.

Chapter 3. Methods

3.1. Introduction

Although many contact models were used in the numerical research of asphalt mixture, few of them can be validated directly by lab experiment. This chapter introduces a lab test which could be used to verify the contact model developed by Zhu et al. The reason this model was chosen is a visco-elastic binder layer was used to bond the two contact particles and the boundary conditions described by the model could be perfectly satisfied by our experiment devices. A cabinet x ray tomography technique was used to build a particle-binder system which matches the geometry of the model described in the paper, the relative normal displacement and resistant force of the system under compression could be recorded during the test. A frictionless boundary is achieved by fixing two particles on the top and bottom plates without contact with test chamber. The details of the model and the lab test are described in the chapter below.

3.2. Normal compliance model

The model analyzes a system with two elastic particles bonded by a thin visco-elastic binder layer. The configuration of this axi-symmetric system is defined in figure 3-1.

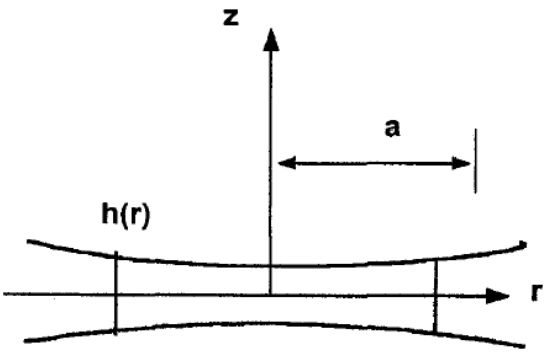

Figure 3-1 binder-particle system (Han et al).

The function z = h(r) represents the geometry of interfacial boundary between the particles and the binder, given by

$$h_r = h_0(1 + d\frac{r^2}{a^2}) \quad \textbf{3-1}$$

where a is the radius of contact area, h_0 is the thickness of the binder at r = 0, and d is the dimensionless shape parameter related to the curvature of particle surface, which is limited in a range 0 < d < 1. For a planar surface, d is zero. For a spherical particle, d is given by

$$d = \frac{a^2}{2Rh_0} \quad \textbf{3-2}$$

where R is the radius of the spherical particles.

Zhu at al (1996) defined the constraint modulus $E_1$and E_2 and Poisson's ratio υ_1, and υ_2 for the particles and the binder respectively, where the constraint modulus E_1, and E_2 are defined as

$$E_i = \frac{2G_i(1-\upsilon_i)}{1-2\upsilon_i}, i = 1,2 \quad \textbf{3-3}$$

and G_1, and G_2 are the shear modulus of the particles and the binder respectively.

For Maxwell binder, the normal stress-strain relationship in the thin layer of binder is given by

$$\dot{\varepsilon}_2(r,t) = \frac{1}{E_2}\dot{p}(r,t) + \frac{1}{\eta_\varepsilon}p(r,t) \quad \textbf{3-4}$$

or in its integral representation

$$\varepsilon_2(r,t) = \frac{p(r,t)}{E_2} + \frac{1}{\eta_\varepsilon}\int_0^t p(r,\tau)d\tau \quad \textbf{3-5}$$

where, $\varepsilon_2(r,t)$ denotes the normal strain and p(r, t) denotes the normal stress in the binder. η_ε is the coefficient of viscosity.

The relative normal approach $\delta_z(t)$ for the two particles is separated into two components, both are time dependent: the normal displacement at the binder-particle interface relative to the particle's centroid, $w_1(r, t)$; and the normal displacement at the binder-particle interface (i.e., at z = h(r) relative to the z = 0 plane), $w_2(r, t)$, given by

$$\delta_z(t) = w_1(r,t) + w_2(r,t) \quad \textbf{3-6}$$

It is approximated that the normal strain is uniform in the z direction across the thin layer of binder. Thus the normal displacement $w_2(r, t)$ can be expressed as follows

$$w_2(r,t) = h(r)\frac{p(r,t)}{E_2} + \frac{h(r)}{\eta_\varepsilon}\int_0^t p(r,\tau)d\tau \quad \textbf{3-7}$$

where p(r, t) is the interfacial normal pressure between the particle and the binder.

The method assumed that the characteristic dimension of the particle is much larger than that of the particle-binder contact area. So $w_1(r, t)$ is pursued based on a half-space premise. Using the well-known Boussinesq equation, $w_1(r, t)$ can be related to p(r, t) by:

$$w_1(r,t) = \frac{1-\upsilon_1^2}{\pi E_1}\int_0^a p(\rho,t)\frac{I(\rho,r)}{\sqrt{\rho^2+r^2}}d\rho \quad \textbf{3-8}$$

Where $I(\rho,r)$ is defined as

$$I(\rho,r) = I(k) = \int_0^{2\pi} \frac{d\theta}{\sqrt{1-k\cos\theta}} \quad \textbf{3-9}$$

$$k = \frac{2r\rho}{r^2+\rho^2} \quad \textbf{3-10}$$

By summing up the two components $w_1(r, t)$ and $w_2(r, t)$, the relative normal approach $\delta_z(t)$ for the two contact bodies is

$$\delta_z(t) = h(r)\frac{p(r,t)}{E_2} + \frac{h(r)}{\eta_\varepsilon}\int_0^t p(r,\tau)d\tau + \frac{1-\upsilon_1^2}{\pi E_1}\int_0^a p(\rho,t)\frac{I(\rho,r)}{\sqrt{\rho^2+r^2}}d\rho \quad \textbf{3-11}$$

Integration of the interfacial pressure function, p(r, t), over the contact area gives the resultant normal contact force $P_z(t)$

$$P_z(t) = 2\pi\int_0^a p(r,t)rdr \quad \textbf{3-12}$$

Equations 3-11 and 3-12 govern the magnitude and distribution of interfacial pressure. The compliance relationship is a time-dependent function that relates the relative normal approach $\delta_z(t)$ and the contact force $P_z(t)$.

3.2.1. Two extreme cases

3.2.1.1 Rigid particle case

In the rigid particle case, the relative movement of the two contact bodies is contributed only from the time-dependent deformation of visco-elastic binder.

$$\delta_z(t) = h(r)\frac{p(r,t)}{E_2} + \frac{h(r)}{\eta_\varepsilon}\int_0^t p(r,\tau)d\tau \quad \textbf{3-13}$$

The corresponding normal interfacial pressures denoted as $p_1(r, t)$, is given by

$$p_1(r,t) = \frac{P_z(t)}{\pi a^2}\frac{h_0}{h(r)X} \quad \textbf{3-14}$$

Where

$$X = \frac{\ln(1+d)}{d} \quad \textbf{3-15}$$

d is the shape parameter defined in equation 3-2, thus the time-dependent normal compliance relationship between the contact force $P_z(t)$ and the relative approach $\delta_z(t)$ becomes

$$\delta_x(t) = C_{1Z}P_Z + C_{1Z}\frac{E_2}{\eta_\varepsilon}\int_0^t P_z(\tau)d\tau \quad \textbf{3-16}$$

$$C_{1Z} = \frac{h_0}{\pi a^2 E_2 X} \quad \textbf{3-17}$$

3.2.1.2 Rigid binder case

In the rigid binder case, the deformation is contributed only from the particle. The normal interfacial pressure denoted as $p_2(r, t)$ corresponding to the rigid punch problem are known to be

$$p_2(r,t) = \frac{P_z(t)}{2\pi a}(a^2 - r^2)^{-1/2} \quad \textbf{3-18}$$

$$\delta_z(t) = C_{2z}P_z(t) \quad \textbf{3-19}$$

$$C_{2z} = \frac{1-\upsilon_1^2}{2aE_1} \quad \textbf{3-20}$$

3.2.2. Best estimated solution:

Zhu et al (1996) developed approximate solutions to represent the upper and lower bound of compliance model, which is:

$$\delta_z(t) \le (C_{1z} + b_1 C_{2z}) P_z(t) + C_{1z} \frac{E_2}{\eta_\varepsilon} \int_0^t P_z(\tau) d\tau \qquad \textbf{3-21}$$

$$\delta_z(t) \ge (b_2 C_{1z} + C_{2z}) P_z(t) + C_{1z} b_2 \frac{E_2}{\eta_\varepsilon} \int_0^t P_z(\tau) d\tau \qquad \textbf{3-22}$$

A suitable form of pressure function was selected which can be substituted directly into the governing equations to obtain the best estimated solution. Where b1=b2=1:

$$\delta_z(t) = (C_{1z} + C_{2z}) P_z(t) + C_{1z} \frac{E_2}{\eta_\varepsilon} \int_0^t P_z(\tau) d\tau \qquad \textbf{3-23}$$

3.3. Experimental validation

The Skyscan 1174 cabinet x-ray tomography system was used in the experiment to verify the normal compliance model introduced before.

3.3.1. X-ray tomography system

The Skyscan 1174 system, shown in figure 3-2, is a compact, cost efficient micro x-ray scanner for nondestructive three-dimensional microscopy. It could be operated by either a portable or a desk-top PC and is supplied with software for system control, X-ray radiography, 3D-reconstruction, 2D/3D image analysis and 3D realistic visualization. The SkyScan-1174 scanner supports variable magnification (6 to 30mm field of view), adjustable source energy (20 to 50KV) and flexible image format. The material testing stage of Skyscan system, shown in Figure 3-3, can perform compression, tension and torsion test. The loading-displacement or the stress-strain curve can be saved as an image or text file. It allows the tomographic scanning of the sample during the test. The testing sample can be held under specific loading for scanning. The testing stage applies displacement to the top and bottom of the sample in equal amount but in opposite directions. This keeps the central part of the sample relatively static for scanning purpose.

Figure 3-2 Skyscan 1174 system

Figure 3-3 Testing stage of the microscopy system (SKYSCAN, 2006)

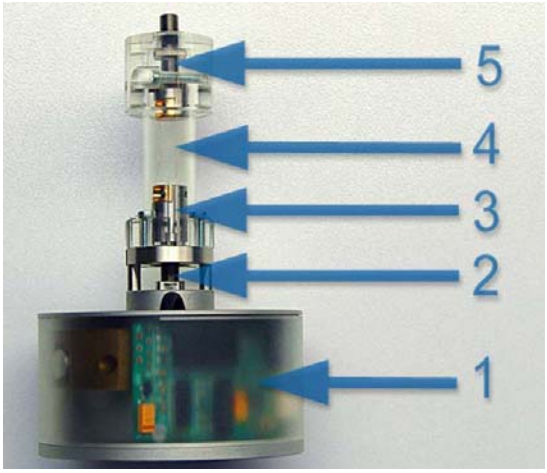

Figure 3-4 Skyscan testing stage illustration

Figure 3-4 above shows each part of the testing stage, the bottom body of the stage (1) contains a microprocessor controller and connector to the socket on the specimen stage in the scanner, a stepper motor drive with gearbox and a solid-state force sensor. The output gear-head (2) imparts a rotation to the two coaxial axles with equal speed but in opposite directions. It allows the stage to apply forces including torque to the top and bottom of the sample in equal amount, but in opposite directions, keeping the central part of the object static for imaging and micro x-ray scanning. The bottom support of the object (3) moves upward during compression, downward during tension and rotates to apply torsion force. The specimen chamber (4) moves together with the supporting metal ring and includes the top object holder (5) which can be adjusted to the particular object length. It moves down during compression, up during tension and turns in the direction opposite to the bottom object holder during torsion loading. The central part of the specimen chamber is a thin-walled tube transparent for x-ray radiation. This is the place for scanning the object under applied load. The specification of Skyscan 1174 is shown in table 3-1 below.

Table 3-1 Skyscan 1174 specifications

SYSTEM:	SkyScan 1174

Maximum scan volume	30mm in diameter, 30mm in length + 50mm vertical travel.
Pixel size	6 to 30µm (1024x1024) or 12 to 60µm (512x512)
X-ray detector	1280x1024 pixel 12-bit X-ray camera in on-chip integration mode with lens coupling to scintillator
X-ray source	20-50kV, 40W sealed air cooled tube
Software package	System control, x-ray imaging, 3D reconstruction, 2D/3D x-ray analysis, realistic 3D visualization. Optional- cluster reconstruction with networked node computers.
Reconstruction algorithm	Volumetric reconstruction - convolution with back-projection for cone-beam (Feldkamp)
Radiation safety	<1uSv/h at any point on the instrument surface
Estimated Maximum force	100 Newtons
Motor speed	1-50 um/s

3.3.2. Sample preparation

Since the size of the chamber is limited for the system, two semi balls are used instead of two whole balls. Glue is used to fix the two semi balls to the object holder respectively with thin asphalt binder layer on each of them, the illustration of the sample prepared are shown in figure 3-5 to figure 3-7.

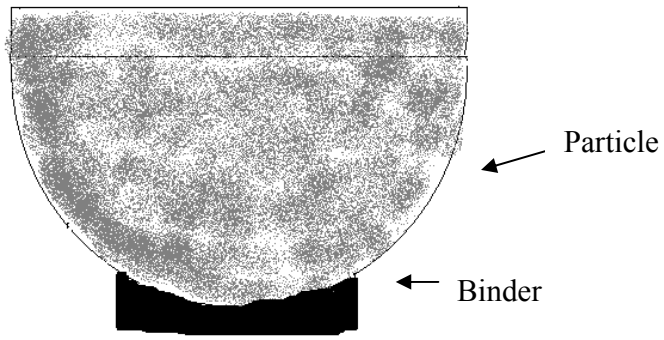

Figure 3-5 sample sketch

Figure 3-6 upper part of sample

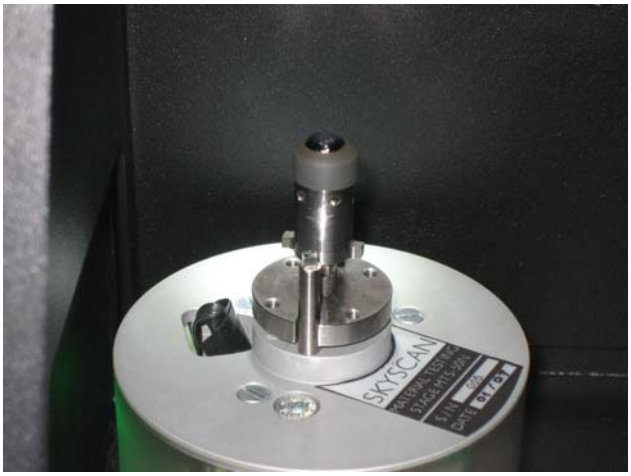

Figure 3-7 lower part of sample

3.3.3. Sample testing

Samples were tested under uniaxial compression loads applied on top and bottom stage. With the help of x-ray scanner, the parameters needed in the compliance model were measured by the tools provided by the software (Figure 3-8). The testing stage is displacement controlled. The displacement speed was chosen according to the allowable range of the testing device, and was set at 17.5μm/s. The resistant force was monitored

and recorded during the loading. (Figure 3-9). When the force reaches the maximum allowable value of the testing stage, the displacement application will stop. For the sample in this study, the application of displacement was stopped when two elastic particles started to contact to each other through the asphalt layer. Prior to each test, the testing stage was calibrated according to the procedure recommended by the manufacturer. Force displacement data was stored as a text file for each sample. The specification of asphalt binder is PG 64-22 coming from the lab of the Virginia Transportation Institute and the temperature at which the experiments are conducted is around 25-27^{o}C given by thermometer. The specifics of the experiment are listed in the table 3-2.

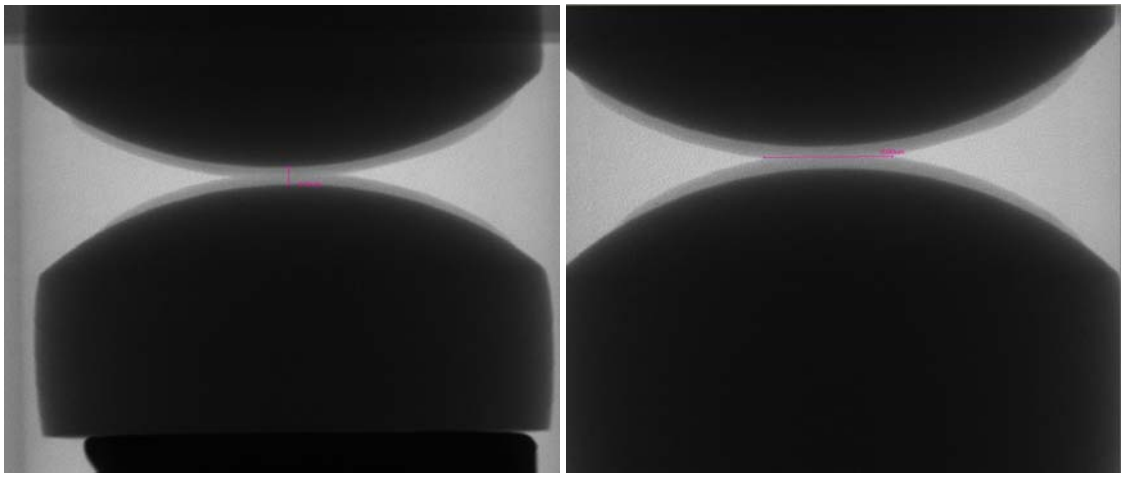

Figure 3-8 Test measurement

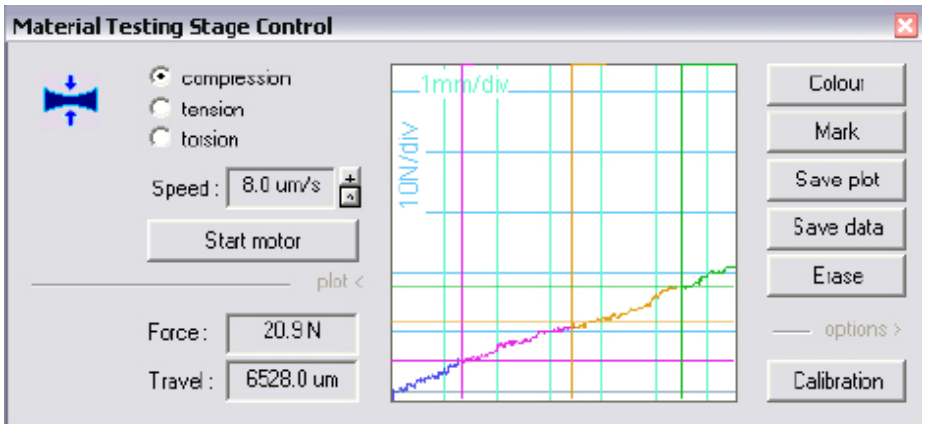

Figure 3-9 Test record

Table 3-2 Experiment specifics

Inner diameter of the chamber	10 mm
Diameter of particle	12.70 mm
Column diameter	9 mm
Material of particle	Polyvinyl Chloride (E=2400-4100 Mpa $\upsilon = 0.41$)
Asphalt binder	PG 64-22
Test temperature	Room Temperature
Loading speed	17.5 um/s

Chapter 4. Results analysis

4.1. Introduction

This chapter analyzes the parameters used in the model and documents the compression test results. The tests were conducted by using three different group of film thickness. The results are used to compare with the theoretical solutions coming from the compliance model. Some correlation analyses are also conducted.

4.2. Parameter definition

Based on the best estimate solution for the particle binder system, the parameters below need to be defined or calculated.

1. The thickness of the binder at r=0 h_0
2. Radius of contact area a
3. Shear modulus for both particle and binder G_1 G_2
4. Possion's ratio for both particle and binder υ_1 υ_2

5. Shape parameter for particles
6. Viscosity of asphalt binder η_{ε}
7. Integration part of the model $\int_0^t P_z(\tau)d\tau$

4.2.1. The thickness of the binder at r=0, h_0

The x-ray imaging program provided with the Skyscan 1174 system has the capability to measure the real distance between two points shown on the picture. The thickness of the binder at r=0, h_0 (Figure4-1) could be measured manually by picking two vertex of both particles on the scanned image instantly during the experiment.

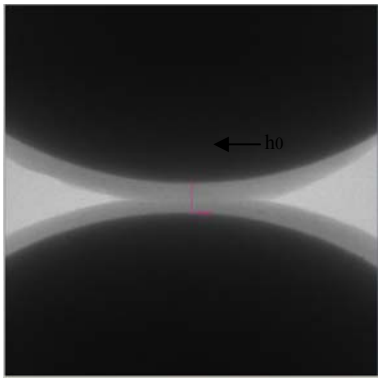

Figure 4-1 thickness measurement

4.2.2. Radius of contact area

Since the contact area between the particle and the binder were keep changing during the compression process, the change of contact area are approximated linearly increasing during the test, thus the radius of contact area used in the model will be a linear function of time determined by the contact areas before and after the test (figure 4-2) and the test time. Both of them could be measured during the test.

$$a = \frac{(a_{after} - a_{before})}{t_{end}} t + a_{before} \qquad \textbf{4-1}$$

where

a_{after} = radius of contact area after test

a_{before} = radius of contact area before test

t_{end} =ending time of the test

t =testing time

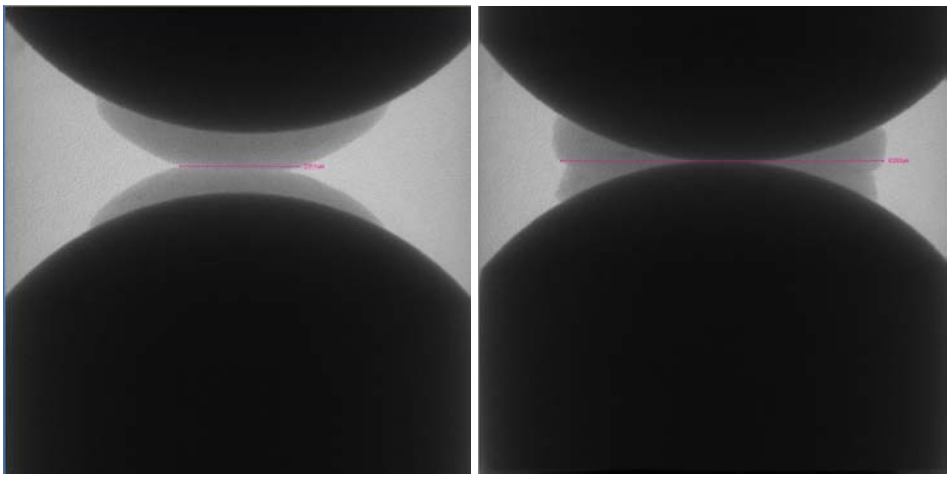

Figure 4-2 Contact area before and after test

4.2.3. Shear modulus and Poisson's ratio for particles and binder

4.2.3.1 Particles

The particles used in the test are made of Polyvinyl Chloride (PVC), which is used in a wide variety of manufactured product. The Young's modulus for this material provided by the Corneliussen (2002), who did extensive research in elastic modulus of the different materials, is at a range of 2400 to 4100 Mpa. And the poisson's ratio given by Harvel Industry Company, which is specialized of making PVC duct, is 0.41 at room temperature.

Based on the relation between the shear modulus G and Young's modulus E given in equation 4-2, we can calculate the shear modulus of the particles and use the equation 3-3 to obtain the constraint modulus E_1.

$$G = \frac{E}{2(1+\upsilon)} \qquad \textbf{4-2}$$

E—Young's modulus

G—Shear modulus

υ— Poission's ratio

4.2.3.2 Binder

For the shear modulus G^*, Glen Alan Malpass (2003) did the DSR tests for aged virgin binder PG64 under different temperatures, the complex modulus G^* at 25°C is around 4.3 Mpa and 2.8 Mpa at 28° C. The range for the phase angle is 53° to 55°. As introduced in the chapter 2, complex modulus G^* can be considered as the total resistance of the binder to deformation when repeatedly sheared. And the storage modulus part can be calculated using the equation 2-3 by given the poisson's ratio. In this study the poisson's ratio is assumed to be 0.35. The constraint modulus of the binder could be obtained by the definition. (Equation 3-3)

4.2.4. Shape parameter and the viscosity

The shape parameter could be calculated directly by its definition in equation 3-2, and the input a and h_0 were obtained from each test. The viscosity of the binder is calculated based on the recommended method provided by the NCHRP report 547, the relationship between the viscosity and the complex modulus is:

$$\eta = \frac{G^*}{10}\left(\frac{1}{\sin\delta}\right)^{4.8628} \qquad \textbf{4-3}$$

Where

η is binder viscosity

G^* is binder complex shear modulus

δ is binder phase angle

4.2.5. Integration part of the model $\int_0^t P_z(\tau)d\tau$

The resistant force and displacement data would be recorded during the test, since the loading speed of each test is constant, the relation between the resistant force and the

time could be obtained by dividing the displacement by the loading speed. The Rimen integration is conducted to obtain the $\int_0^t P_z(\tau)d\tau$. The areas of each rectangle surround by the two consecutive force values and the time axis were calculated and then accumulated to get the integration value for each point of interest.

4.3. Compression test results

4.3.1. Introduction

In order to investigate the thickness effect of the asphalt binder to the contact behavior of aggregates, three groups of compression test were contact using samples with different binder film thicknesses.

4.3.2. Test 1

Film thickness could have influence to the mechanical behavior of the particle binder system. There samples with different binder film thickness were tested. The thicknesses of the film were controlled manually and measured by the program. The samples with film thickness larger than 1mm are shown in figure 4-3, and the results data are listed in the table 4-1.

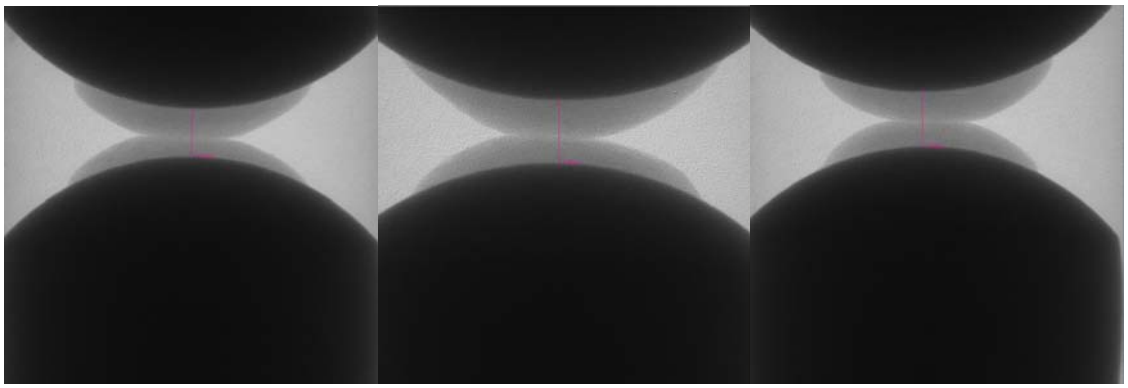

(a) (b) (c)

Figure 4-3 Samples of Test 1 with different film thicknesses (a) 1.145 mm (b) 1.203 mm (c) 1.313 mm

Table 4-1 Results data of Test 1

h_0=1.145		h_0=1.203		h_0=1.313	
Displacement (mm)	Force(N)	Displacement (mm)	Force (N)	Displacement (mm)	Force (N)
0	0	0	0	0	0
0.018	0.4	0.018	0.4	0.035	0.4
0.07	0.7	0.14	0.7	0.525	0.9
0.14	0.9	0.525	0.9	0.613	1.1
0.21	1.3	0.6	1.1	0.753	1.3
0.473	1.5	0.735	1.5	1.12	1.8
0.49	1.8	0.753	1.8	1.138	2
0.927	2	1.103	2	1.155	2.2
0.963	2.2	1.155	2.2	1.295	2.4
1.033	2.6	1.173	2.4	1.313	2.6
1.05	2.9	1.19	2.6		
1.068	3.1	1.208	3.1		
1.138	3.3				
1.155	3.7				

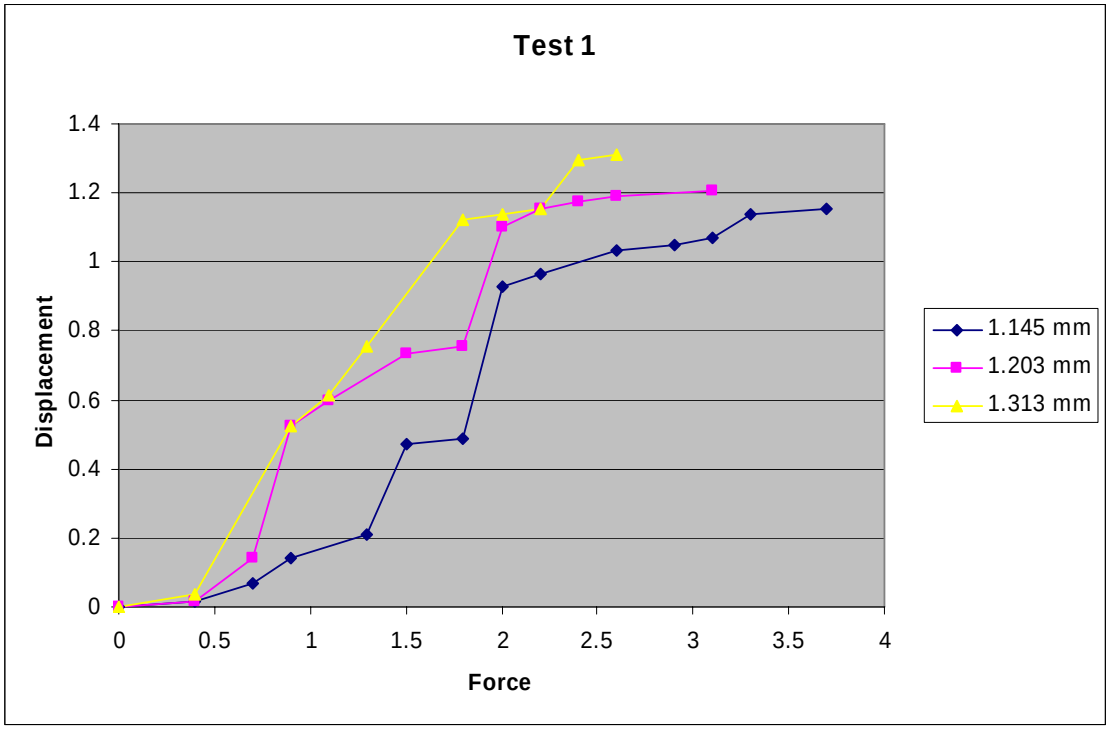

Figure 4-4 Results of Test 1

As shown in the figure 4-4, the relative displacement increases as the force increase, and the thinner film layer is, the larger force is needed to reach a same displacement.

The parameters used and calculated for the compliance model are listed below in the table 4-2:

Table 4-2 Parameters for Test 1

Parameter used	Film thickness h_0		
	1.145 mm	1.203 mm	1.313mm
Complex modulus of the binder (G^*) Mpa	4.3	4.3	4.3
Phase angle of the binder (δ) ^{o}	53	53	53
Poisson's ratio of the binder (υ)	0.35	0.35	0.35
Elastic modulus of the particle (E) Mpa	4100	4100	4100
Poisson's ratio of the particle (υ)	0.41	0.41	0.41
Particle Radius (R) mm	12.7	12.7	12.7
Parameter calculated			
Constraint Modulus of the particles (E_1) Mpa	9531	9531	9531
Shape parameter of the particle (d)	0.636	0.554	0.540
Constraint Modulus of the binder (E_2) Mpa	11.21	11.21	11.21
Viscosity of the binder (η) Mpa	1.28	1.28	1.28
C_{1z} mm/N	0.002269	0.002532	0.002587
C_{2z} mm/N	1.028E-8	1.028E-8	1.028E-8

Based on the information provided above, the predicted results obtained from the compliance model are compared with the test results, shown below in Figure 4-6, the D means normal displacement and F means force. Same notations are used in the future.

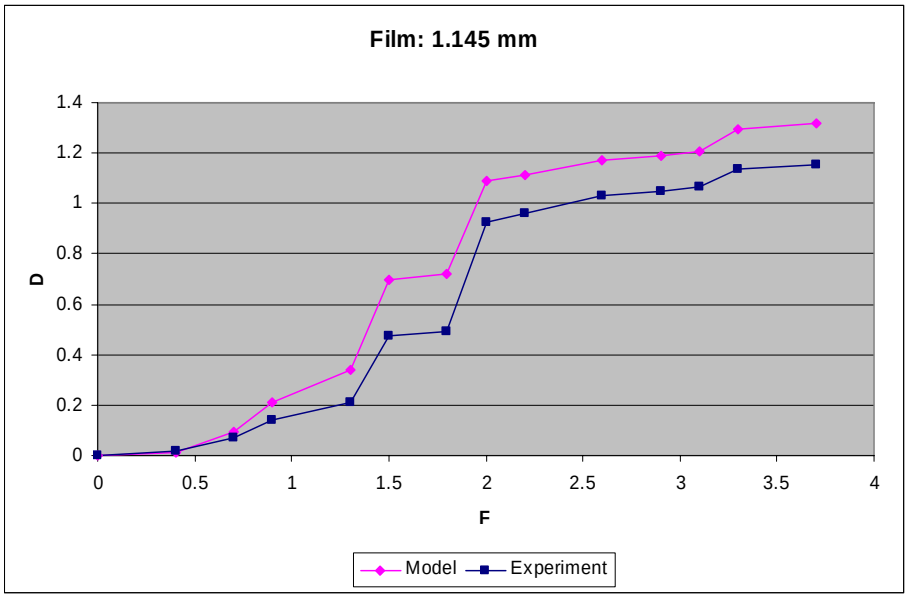

Figure 4-5 Results comparison of 1.145mm film

From the figure 4-5, the experiment results have a good agreement with the model predicted values before the relative displacement value reached to 1 mm, after which, the predicted results are always larger than the experiment results when the test continues. Some correlation analyses are conducted below.

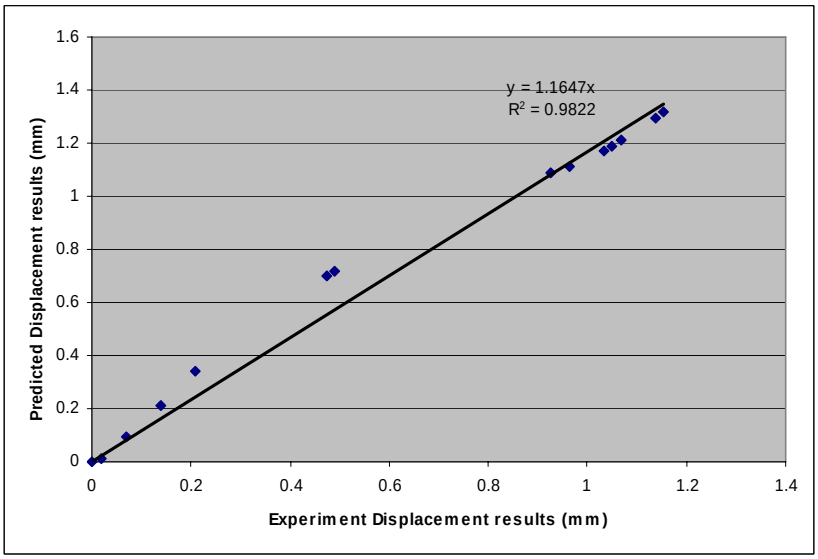

Figure 4-6 Correlation analysis of 1.145mm film

The correlation coefficient is calculated using the equation below.

$$\rho_{x,y} = \frac{E((X-\mu_x)(Y-\mu_y))}{\sigma_x \sigma_y} \quad \text{4-4}$$

Where

X- Experiments results

Y- Predicted results

μ_x - Expected values of X

μ_y - Expected values of Y

σ_x - Standard deviation of X

σ_y - Standard deviation of Y

The correlation coefficient for the 1.415 mm film layer is $\rho_{x,y} = 0.993$

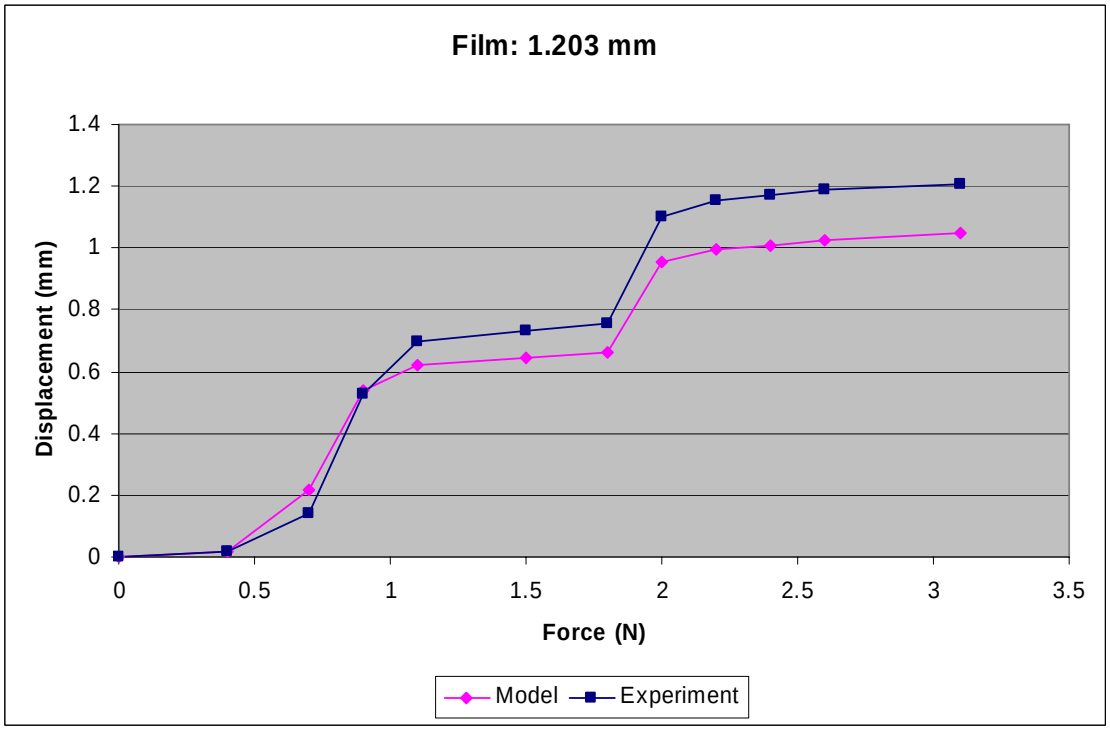

Figure 4-7 Results comparison for 1.203 mm film

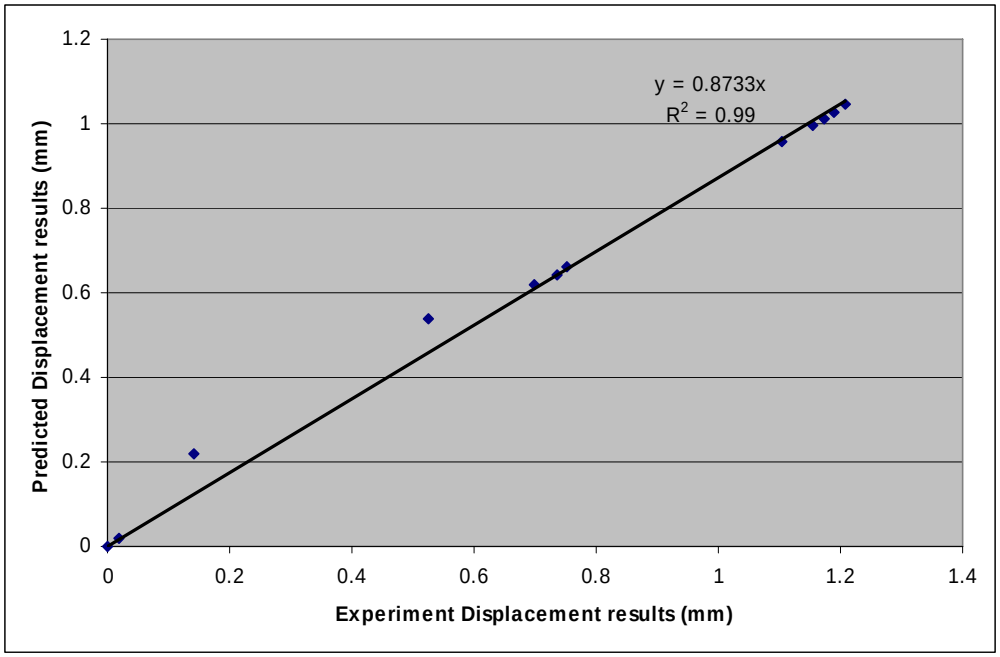

Figure 4-8 Correlation analysis for the 1.203 film

The correlation coefficient of the 1.203 film case is $\rho_{x,y} = 0.973$

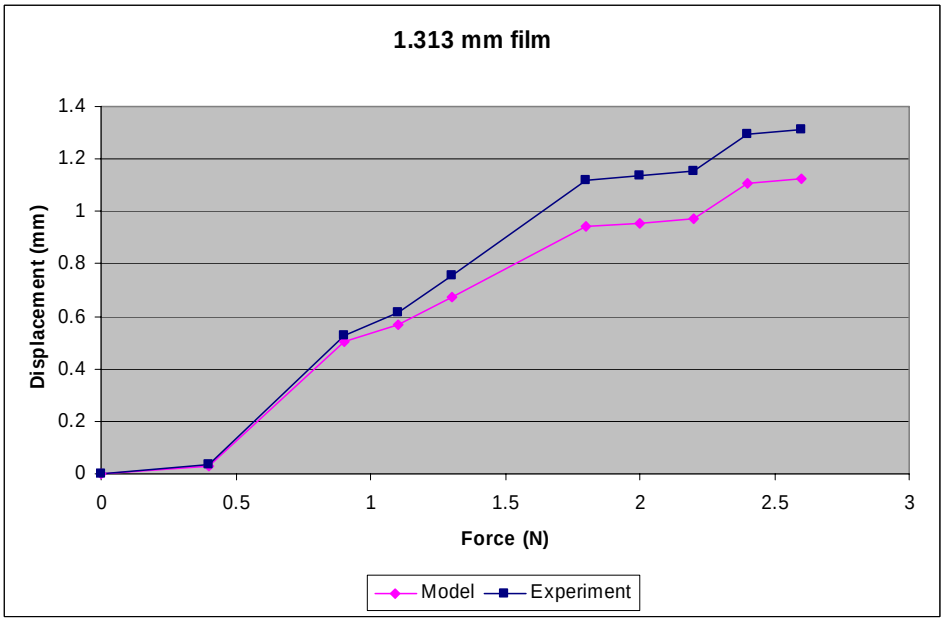

Figure 4-9 Results Comparison for the 1.313 film

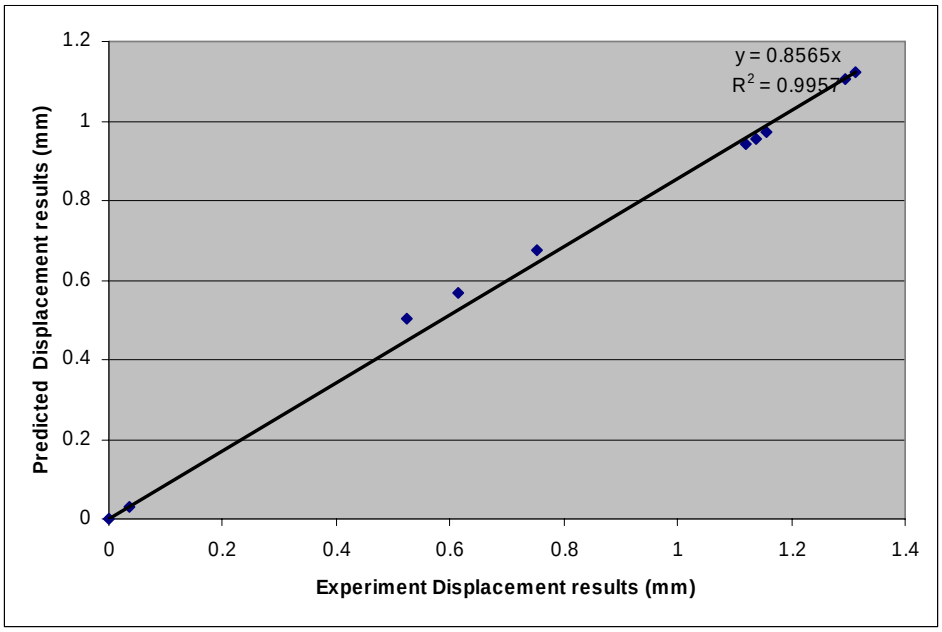

Figure 4-10 Correlation analysis for the 1.313 film

The correlation coefficient of the 1.313 film case is $\rho_{x,y} = 0.998$

4.3.3. Test 2

Same compression test were conducted with a film thickness range from 0.5 mm to 1mm shown in figure 4-11 and table 4-3 shows the results data for test two.

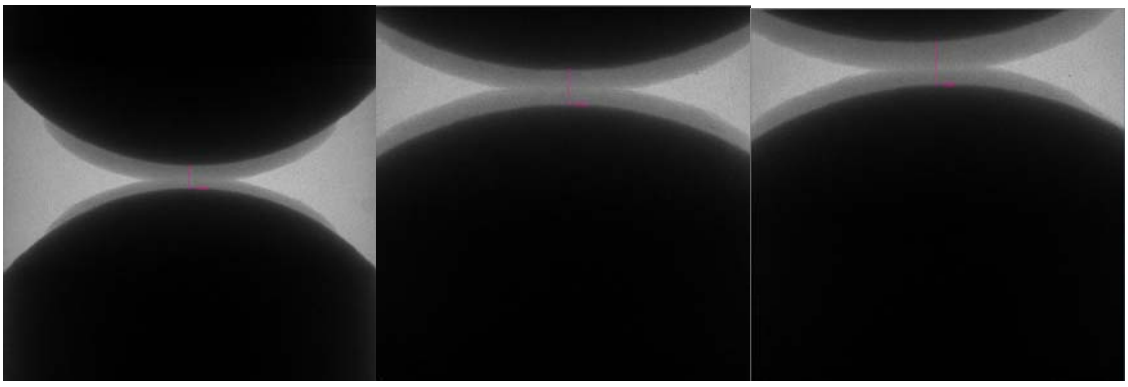

(a) (b) (c)

Figure 4-11 Samples of Test 2 (a) 0.535 mm (b) 0.573 mm (c) 0.7 mm

Table 4-3 Results data of Test 2

h_0=0.535 mm		h_0=0.573 mm		h_0=0.7 mm	
Displacement (mm)	Force (N)	Displacement (mm)	Force (N)	Displacement (mm)	Force (N)
0	0	0	0	0	0
0.018	0.2	0.018	0.2	0.123	0.2
0.035	0.7	0.14	0.4	0.32	1.1
0.07	1.1	0.158	0.7	0.41	1.3
0.193	1.3	0.28	0.9	0.542	1.8
0.245	1.5	0.333	1.3	0.595	2.2
0.315	1.8	0.367	1.5	0.665	2.6
0.385	2.2	0.403	1.8	0.683	3.1
0.42	2.4	0.42	2.4	0.7	3.5
0.455	2.6	0.455	2.6		
0.46	2.9	0.49	3.1		
0.508	3.3	0.508	3.3		
0.542	4	0.56	3.5		
		0.578	4.2		

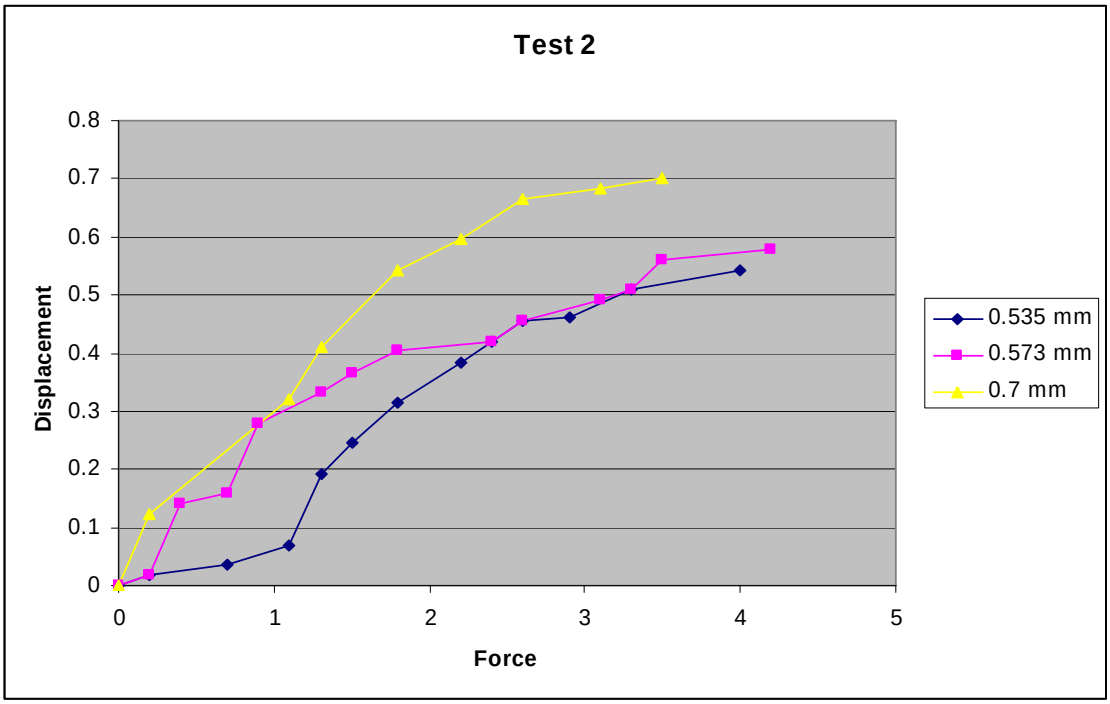

Figure 4-12 Results of Test 2

The parameters used and calculated for the compliance model are listed below in the table 4-4:

Table 4-4 Parameters for test 2

Parameter used	Film thickness h_0		
	0.535 mm	0.575 mm	0.700mm
Complex modulus of the binder (G^*) Mpa	4.3	4.3	4.3
Phase angle of the binder (δ) ^{o}	53	53	53
Poisson's ratio of the binder (υ)	0.35	0.35	0.35
Elastic modulus of the particle (E) Mpa	4100	4100	4100
Poisson's ratio of the particle (υ)	0.41	0.41	0.41
Particle Radius (R) mm	12.7	12.7	12.7
Parameter calculated			
Constraint Modulus of the particles (E_1) Mpa	9531	9531	9531
Shape parameter of the particle (d)	0.636	0.554	0.540
Constraint Modulus of the binder (E_2) Mpa	11.21	11.21	11.21
Viscosity of the binder (η) Mpa	1.28	1.28	1.28
C_{1z} mm/N	0.001474	0.002532	0.001534
C_{2z} mm/N	1.028E-8	1.028E-8	1.028E-8

The test results are compared with predicted results from the model and correlation analysis are conducted below.

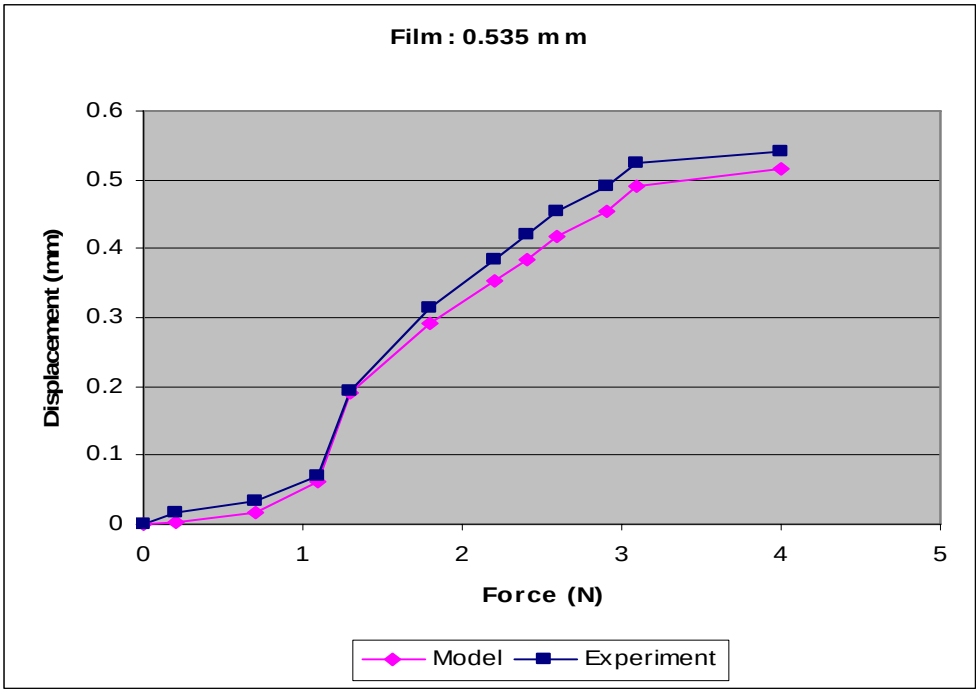

Figure 4-13 Results comparison for 0.535 mm film

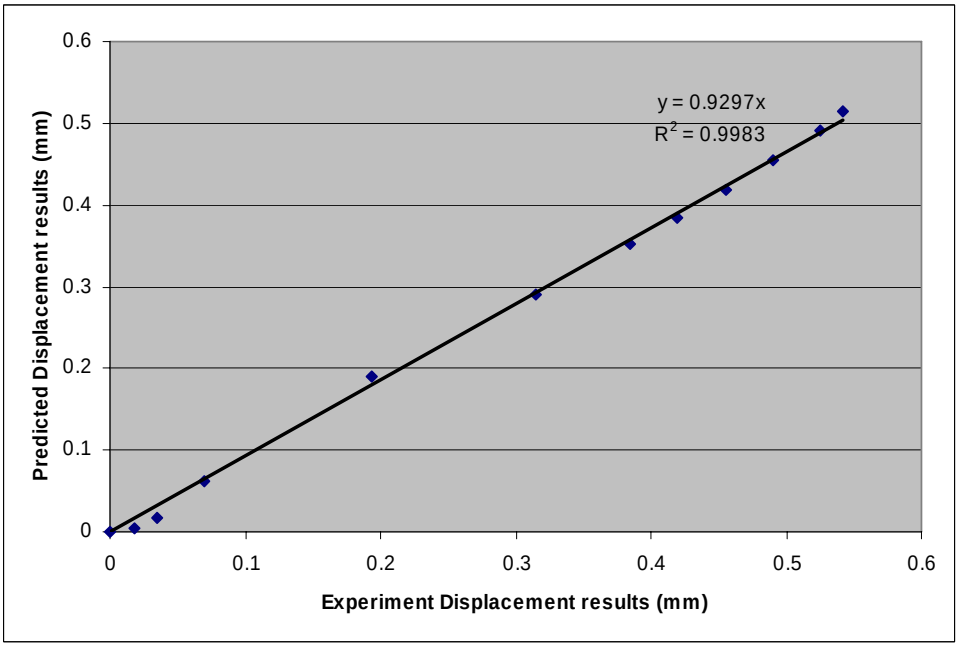

Figure 4-14 Correlation analysis for 0.535 mm film

The correlation coefficient for the 0.535 mm film case is $\rho_{x,y} = 0.999$

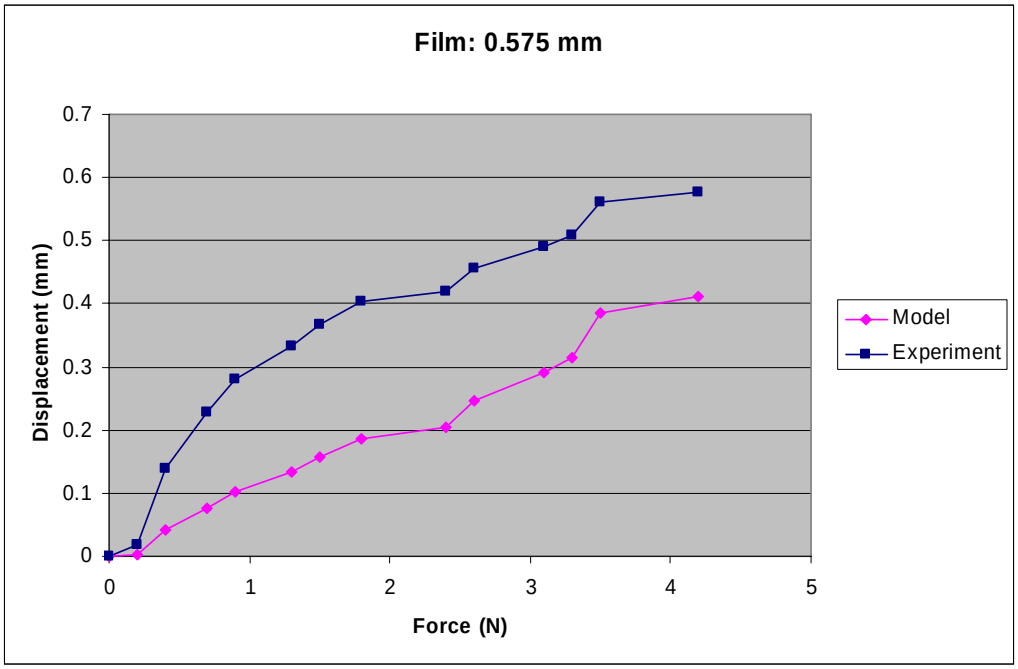

Figure 4-15 Results comparison for 0.575 mm film

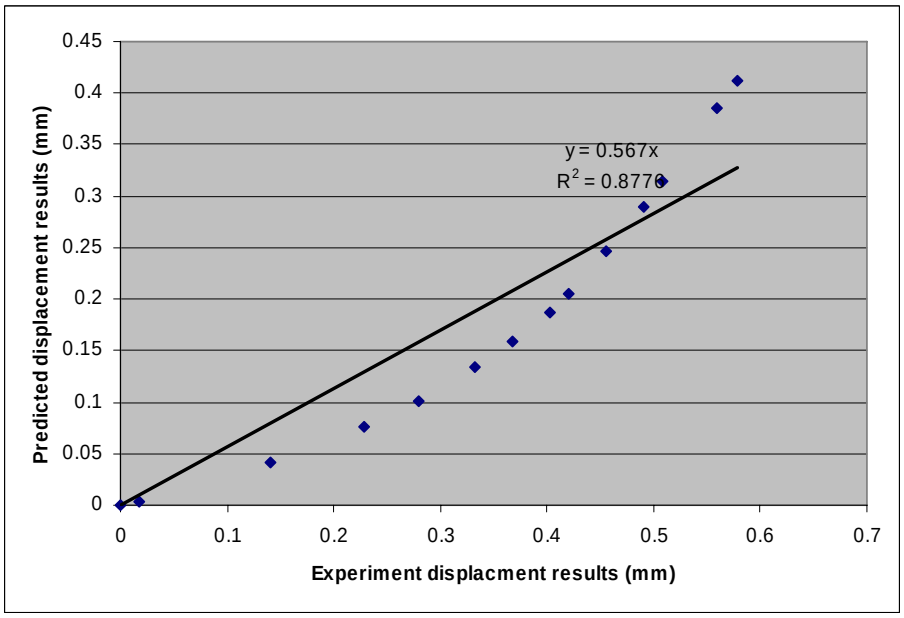

Figure 4-16 Correlation analysis for 0.575 mm film

The correlation coefficient for the 0.575 mm film is $\rho_{x,y} = 0.954$.

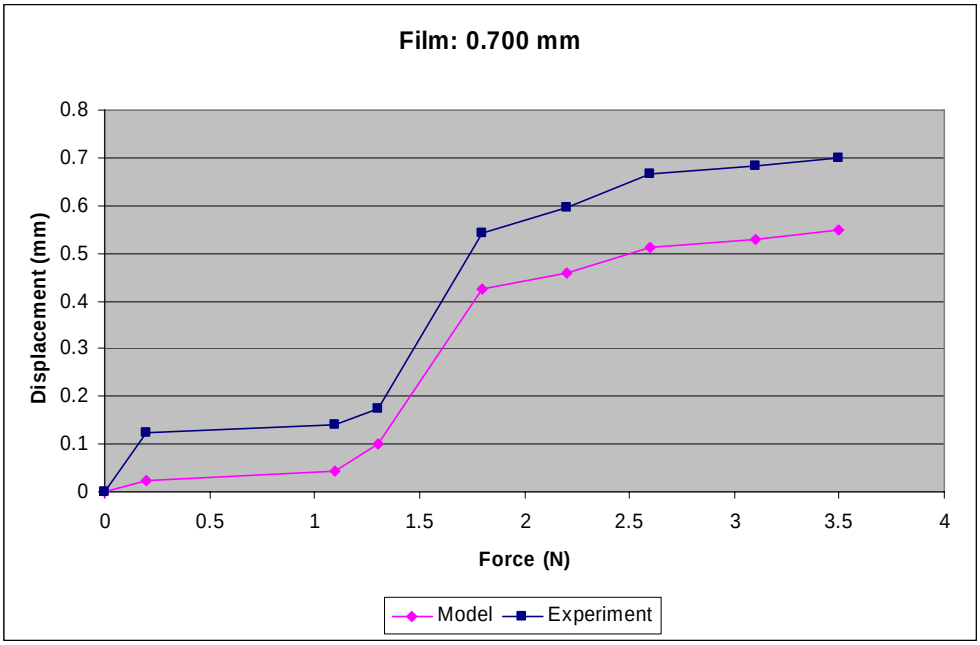

Figure 4-17 Results comparison for the 0.7mm film

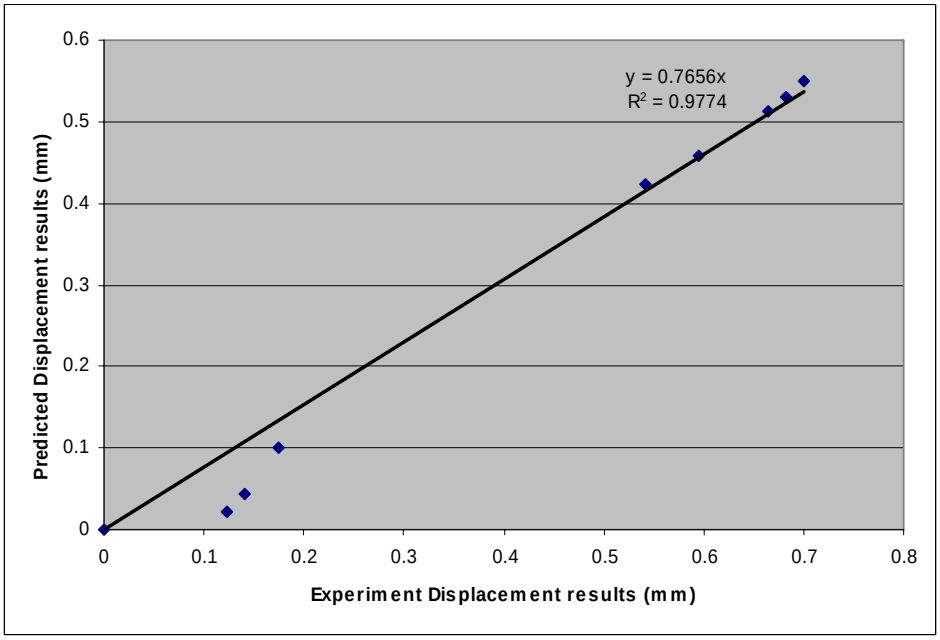

Figure 4-18 Correlation analysis for the 0.7 mm film

The correlation coefficient for the 0.7mm film is $\rho_{x,y} = 0.995$

4.3.4. Test 3

Same compression test were conducted for the film thickness smaller than 0.5 mm. Samples are shown in the figure 4-19 and results data listed in the table 4-5.

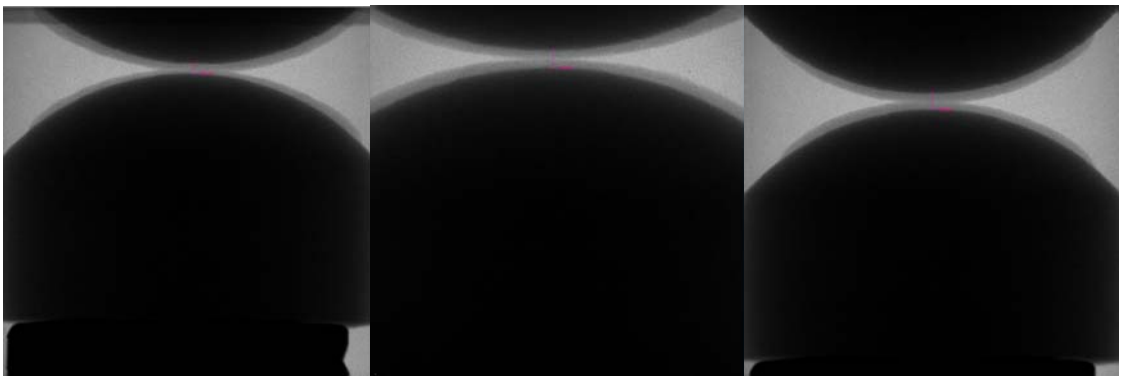

(a) (b) (c)

Figure 4-19 Samples for test 3 (a) 0.252 mm (b) 0.283 mm (c) 0.399 mm

Table 4-5 Results data for test 3

h_0=0.252 mm		h_0=0.283 mm		h_0=0.399 mm	
Displacement (mm)	Force (N)	Displacement (mm)	Force (N)	Displacement (mm)	Force (N)
0	0	0	0	0	0
0.018	1.1	0.018	0.6	0.018	0.4
0.053	1.8	0.175	1	0.14	0.7
0.088	2	0.193	1.2	0.175	0.9
0.158	2.4	0.228	1.8	0.228	1.1
0.21	3.3	0.263	2	0.245	1.3
0.245	3.5	0.297	2.4	0.263	1.5
0.263	3.7			0.297	2
				0.315	2.4
				0.333	2.9
				0.385	3.5
				0.403	4

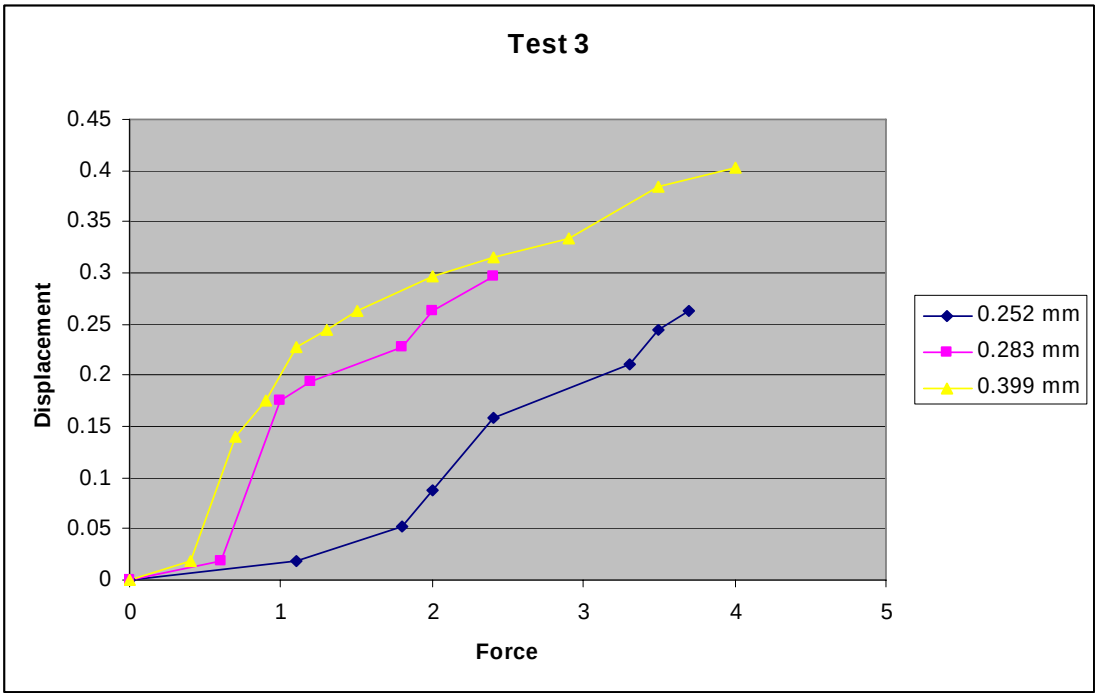

Figure 4-20 Results of test 3

Similar with before, the test results are compared with the predicted results got from the model and the correlation analysis were conducted. The parameters used in the model area listed in the table 4-5.

Table 4-6 Parameters for test 3

Parameter used	Film thickness h_0		
	0.252 mm	0.283 mm	0.399 mm
Complex modulus of the binder (G^*) Mpa	4.3	4.3	4.3
Phase angle of the binder (δ) ^{o}	53	53	53
Poisson's ratio of the binder (υ)	0.35	0.35	0.35
Elastic modulus of the particle (E) Mpa	4100	4100	4100
Poisson's ratio of the particle (υ)	0.41	0.41	0.41
Particle Radius (R) mm	12.7	12.7	12.7

Parameter calculated			
Constraint Modulus of the particles (E_1) Mpa	9531	9531	9531
Shape parameter of the particle (d)	0.636	0.554	0.540
Constraint Modulus of the binder (E_2) Mpa	11.21	11.21	11.21
Viscosity of the binder (η) Mpa	1.28	1.28	1.28
C_{1z} mm/N	0.001203	0.001478	0.001575
C_{2z} mm/N	1.028E-8	1.028E-8	1.028E-8

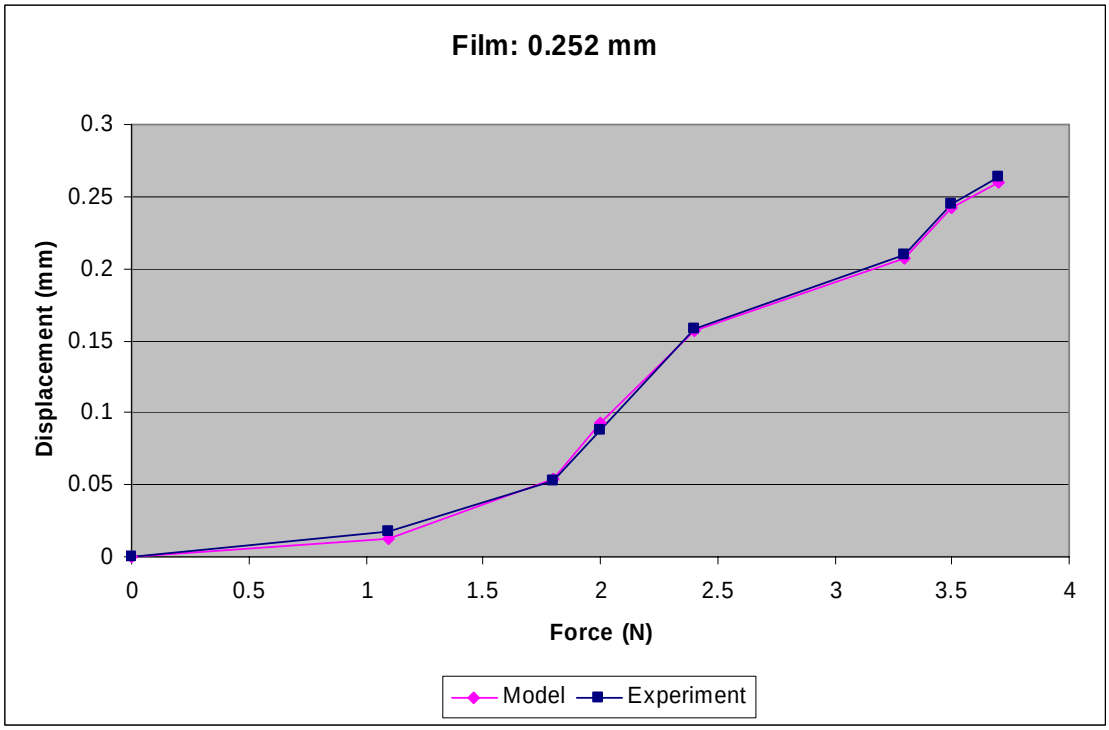

Figure 4-21 Results comparison for 0.252 mm film

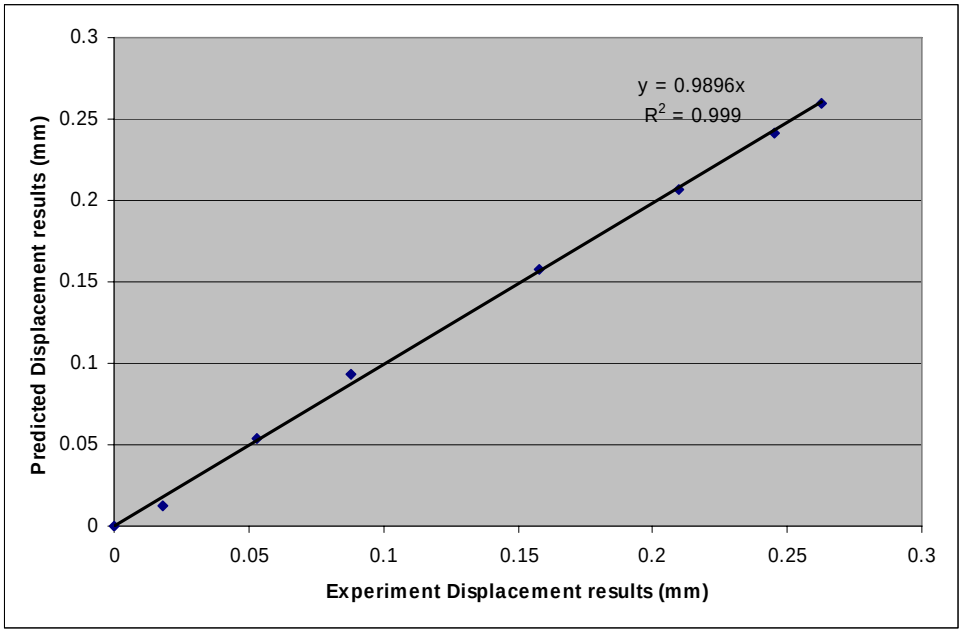

Figure 4-22 Correlation analysis for 0.252 mm film

The correlation coefficient of the 0.252 mm film case is $\rho_{x,y} = 0.999$

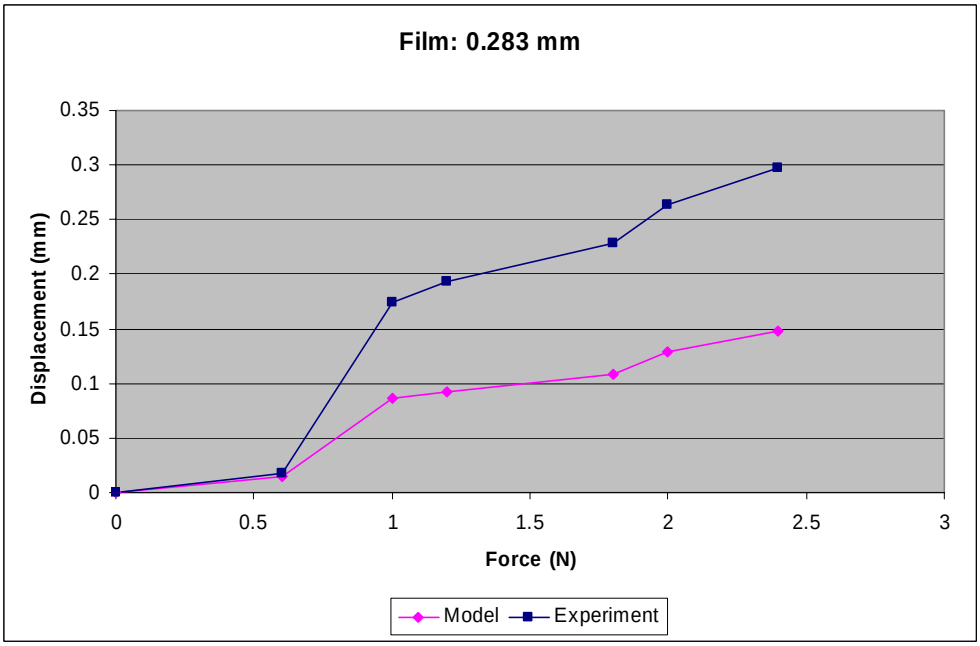

Figure 4-23 Results comparison for 0.283 mm film

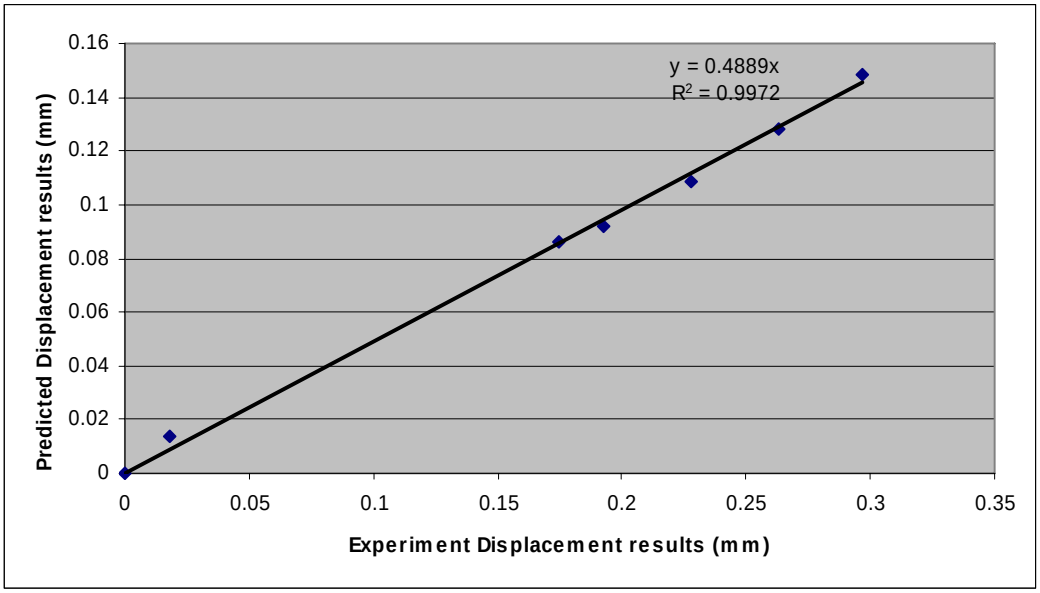

Figure 4-24 Correlation analysis for 0.283 mm film

The correlation coefficient of the 0.283 mm film is $\rho_{x,y} = 0.998$

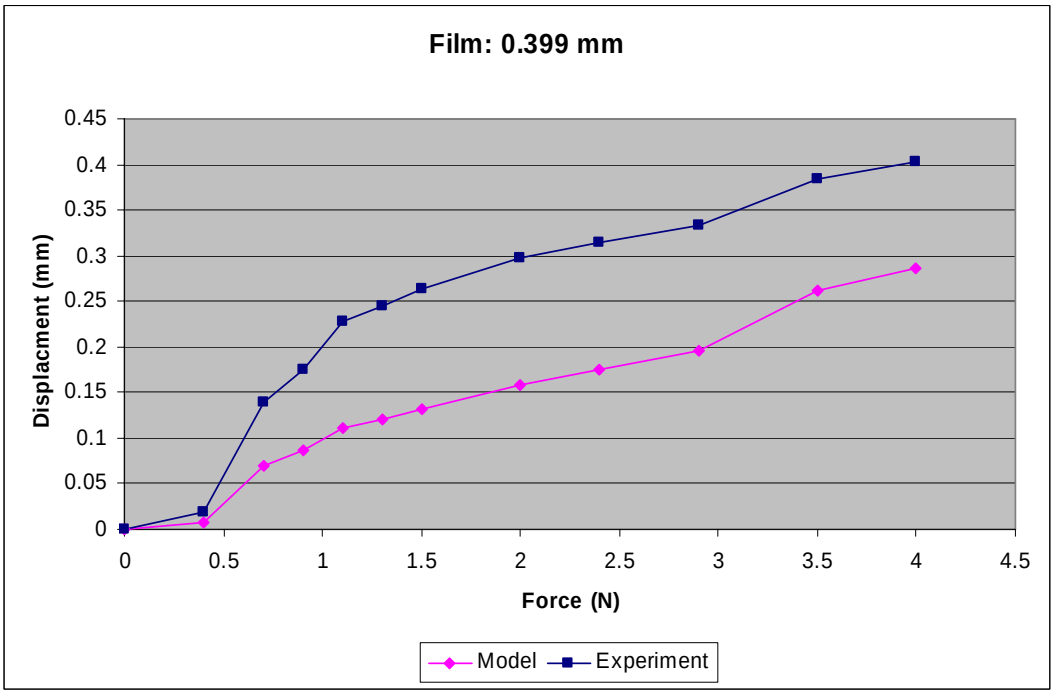

Figure 4-25 Results comparison for 0.399 mm film

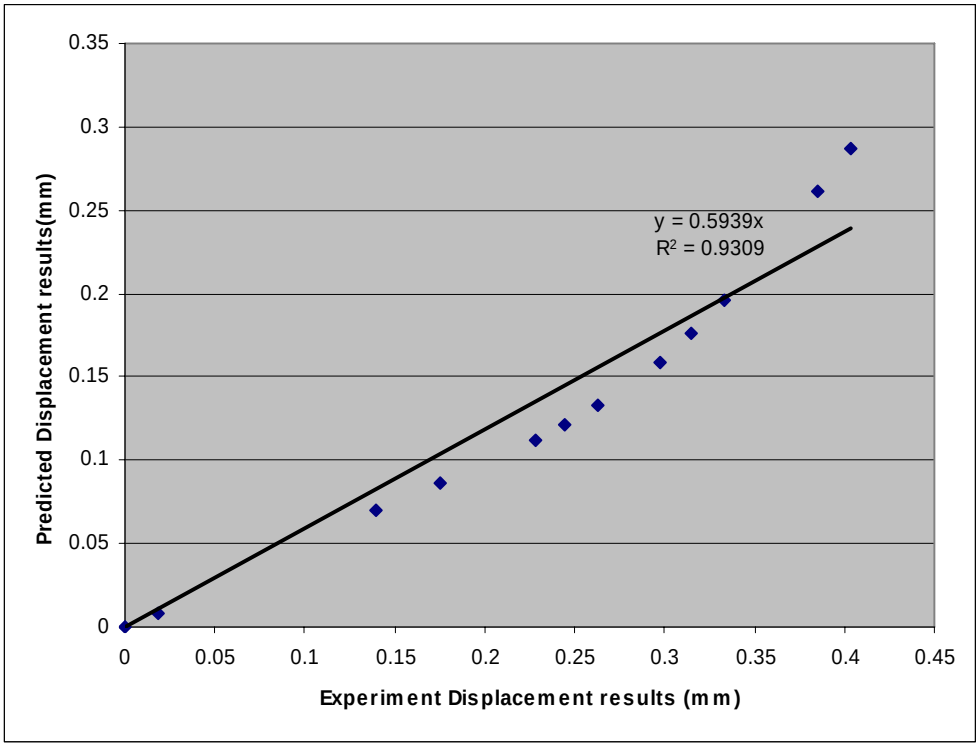

Figure 4-26 Correlation analysis for the 0.399 mm film

The correlation coefficient for the 0.399mm film case is $\rho_{x,y} = 0.971$

4.3.5. Parametric analysis

Some parameters used in the compliance model have a range to choose from, such as the complex modulus and poisson's ratio of asphalt binder, the elastic modulus of the particles. To identify the influences, some parametric analyses were conducted. The test results from test 2 will be used in the parameter study.

4.3.4.1 Elastic modulus of the particles

As mentioned previous in this chapter, the possible range for the elastic modulus of the PVC particle is from 2400 Mpa to the 4100 Mpa, in all the previous study, 2400Mpa was used as the elastic modulus of the particle and obtained compliance C_{2z}=1.028 E-8 mm/N, which hardly has any influence to the performance of the model. If the elastic modulus of the particle is increased to 4100 Mpa, the compliance value C_{2z}

would have an even smaller value which will have no influence of the model at all. So, for this study, instead of using the best estimation solution of this system, the extreme case that the particle is rigid is used, which is shown in the equation 3-16.

4.3.4.2 Complex modulus of the binder

As mentioned in the beginning of this chapter, the DSR test results done by Malpass (2003) for aged virgin binder PG64 under different temperatures was used. The complex modulus G^* at 25°C is around 4.3 Mpa and 2.8 Mpa at 28°C. In the previous model, 4.3 Mpa was used as the complex modulus of the binder. Since the room temperature of our lab is around 26 °C to 27 °C, the temperature influence to the model must be analyzed. By decreasing the complex modulus used in the model from 4.3 Mpa to 2.8 Mpa, which are under the 28 °C and 25 °C respectively, the summation of squared difference (SSD) between each predicted results is calculated and corresponding experiment results using Equation 4-5. Comparing the obtained SSD of models with different complex modulus, the temperature influence of the binder could be studied.

$$SSD = \sum[(y_{P1} - y_{t1})^2 + (y_{P2} - y_{t2})^2 + ... + (y_{Pn} + y_{tn})^2] \quad \textbf{4-5}$$

Where:

SSD= Summation of the Squared difference

y_{pn} = Predicted displacement value obtained from the model

y_{tn} = Displacement value got from the test

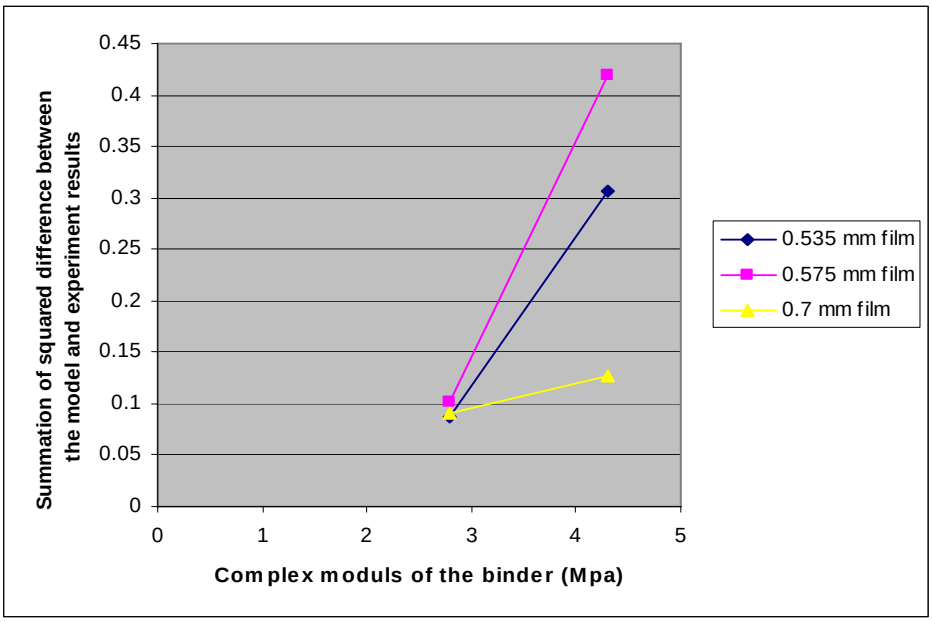

Figure 4-27 Parameter study: binder modulus

As figure 4-27 shown above, the summation of the squared difference between the model and test results are increasing as complex modulus increases, which means the binder compliance model performs better when the complex modulus is lower.

4.3.4.3 Phase angle of the binder

Similar with the previous study, the influence of the binder phase angle to the model are also studied. In our model before, we used the 53^{o} as the phase angle of the binder, but based on the literature review mentioned at the beginning of this chapter, the phase angle is at a range from 53^{o} to 55^{o} in the room temperature. So, we calculated the summation of the difference between the predicted results and the experiment results is calculated when changing the phase angle value used in the model. And from the results below, It can be seen that the summation of the squared difference between the model and experiment results decreases as the phase angle values increases, which means the compliance model perform better when larger phase angle values are used.

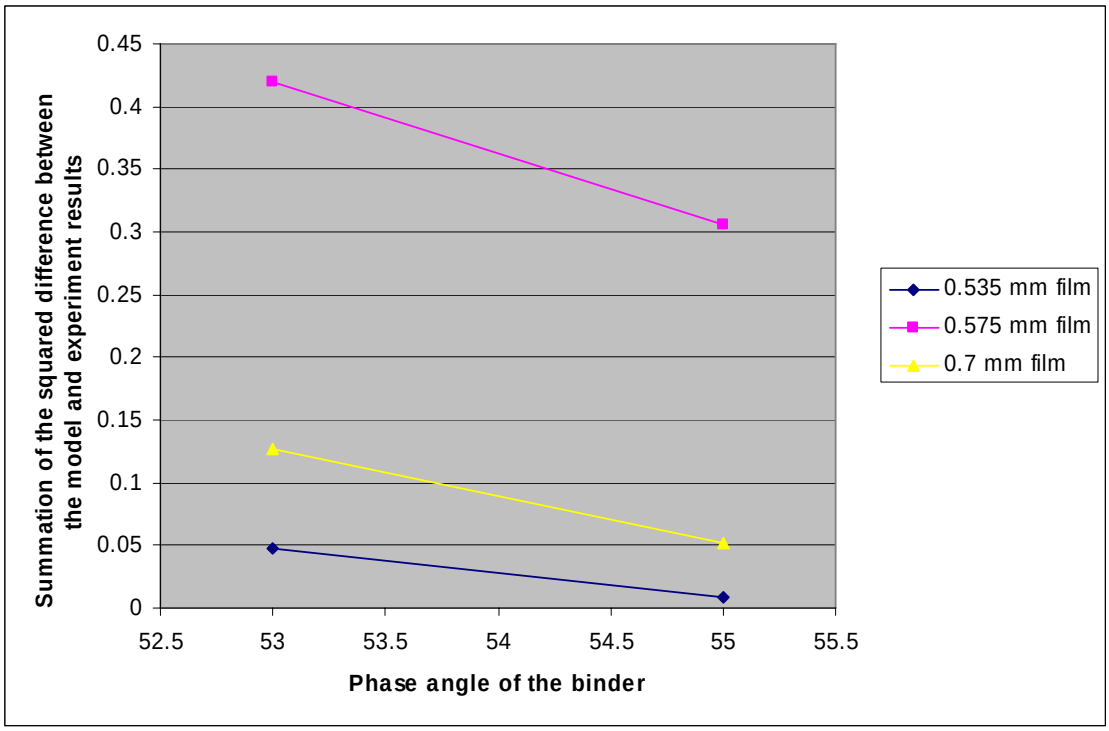

Figure 4-28 Parameter study: binder phase angle

Chapter 5. Conclusion and Recommendation

5.1. Conclusions

Average displacement-force curves for three groups of compression tests with different film thicknesses are shown in the Figure 5-1 below. The results show that, moving same displacement, the resistant force of thinner binder film system is lager thant the mix with thicker binder film, which means the aggregate binder mixture will become stiffer if the film thicknesses decrease. The equations of the trend line from the comparison between the test results and the theoretical solutions and the correlation coefficients of three groups of tests are listed below in the table 5-1.

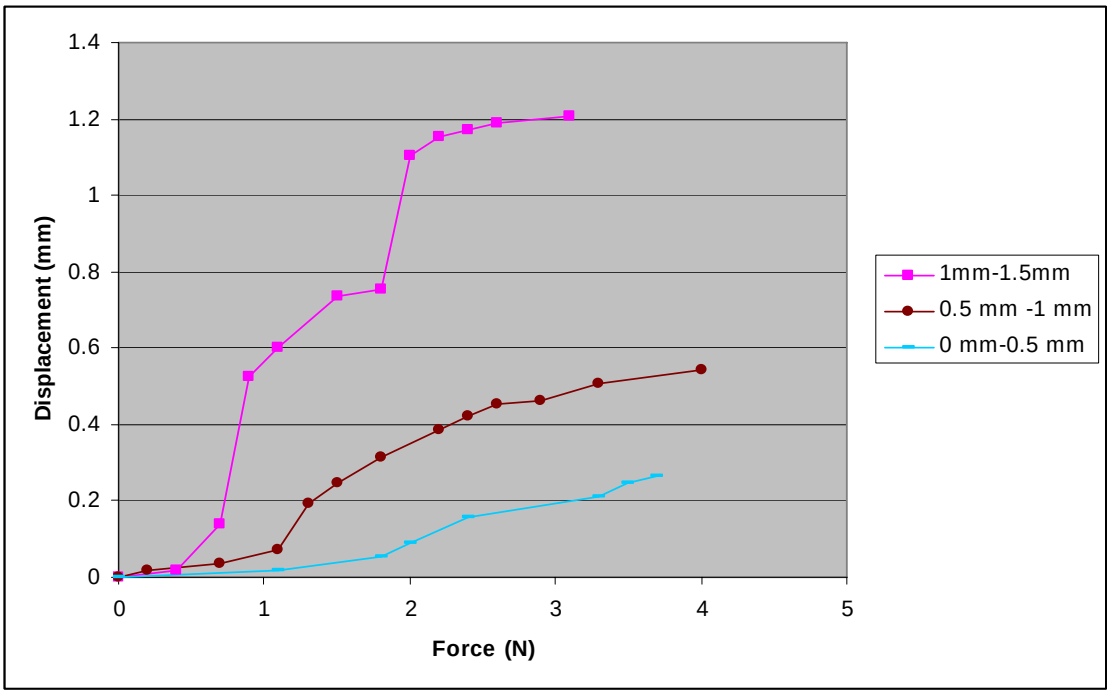

Figure 5-1 Displacement- Force curves of all the tests

Test 1			
Film thickness (mm)	1.145	1.203	1.313
Trend line equation	y=1.2978x	y=1.4423x	y=1.3707x
Correlation coefficient	0.992	0.973	0.974
Test 2			
Film thickness (mm)	0.535	0.575	0.700
Trend line equation	y=1.2904x	Y=0.7774x	Y=1.2436x
Correlation coefficient	0.984	0.925	0.987
Test 3			
Film thickness (mm)	0.252	0.283	0.399
Trend line equation	y=1.2963x	y=0.7337x	y=0.8257xx
Correlation coefficient	0.991	0.971	0.923

Table 5-1 Results conclusion for three tests

Based on the results listed above, the test results and the theoretical results are strong correlated. The equations of trend line between the test results and the predicted results showed that this compliance model is reliable if the stress level is not too high.

5.2. Limitations of the method

- The temperature of the test can not be changed easily.
- Some noises will be produced if using different displacement speed other than recommended in the experiment.
- The thickness of the film is controlled manually, hard to get a specific value.
- Errors introduced when selecting the measuring point on the screen.

5.3. Recommendations for the further study

The Maxwell model could be replaced by some other vico-elastic model like Kelvin model or the models combine the Maxwell and Kelvin element together like

Burger model, Generalized Kelvin model and Generalized Maxwell model. The model of the two particles and binder system could also be modified by some mathematical methods so that could be used in the multiple particles binder system. The irregularity of the aggregate shape should also be considered in the further study. Proper simulation tools should be chosen to develop a contact model for the asphalt mixture.

References

Abbas, A., Papagiannakis, A.T. and Masad, E. (2004). "Linear and Non-Linear Viscoelastic Analysis of the Microstructure of Asphalt Concretes." Journal of Materials in Civil Engineering, ASCE, Vol. 16, pp. 133-139.

Alar, Abbas. (2004) "Simulation of the micromechanical behavior of asphalt mixtures using the discrete element method." Doctoral dissertation submitted to the Department of Civil and Environmental Engineering of Washington State University.

Bahia, H.U., Zhai, H., Bonnetti, K., and Kose, S. (1999). "Non-Linear Viscoelastic and Fatigue Properties of Asphalt Binders." Journal of the Association of Asphalt Paving Technologists, AAPT, Vol. 68, pp. 1-34.

Buttlar, W.G. and You, Z. (2001). "Discrete Element Modeling of Asphalt Concrete: Microfabric Approach." Transportation Research Record 1757, TRB, National Research Council, Washington, D.C., pp. 111-118.

Chang, C. S., Shi, Q., and Zhu, H., "Micro-mechanical Modeling for Elastic Moduli of Bonded Granules." Journal of Engineering Mechanics, ASCE Publication, Vol. 125, No. 6, 1999, pp. 648-653.

Cheung, C Y., Cocks, A C F,.and Cebon, D., (1997) "Isolated contact model of a idealized Asphalt mix." Submitted to the International Journal of Mechanical Science.

Cheung, C.Y. and Cebon, D. (1997). "Thin Film Deformation Behavior of Power-Law Creeping Materials." Journal of Engineering Mechanics, Vol. 123-11, pp. 1138-1152.

Dai, Qingli., Sad,M,H., (2003) "Micromechanicl simulation of asphalt samples using a finite element network model." 16th ASCE Engineering Mechanics Conference July 16-18, University of Washington, Seattle

Ghassan R. Chehab, and Y. Richard Kim. (2005) "Viscoelastoplastic Continuum Damage Model Application to Thermal Cracking of Asphalt Concrete." Journal of materials in civil engineering, pp.384-392

Huang, Baoshan., Mohammad, Louay N. and G. Wije Wathugala. (2004) "Application of a Temperature Dependent Viscoplastic Hierarchical Single Surface Model for Asphalt Mixtures." Journal of Materials in Civil Engineering, March/April, pp.147-154.

Levenberg,E., Uzan, J. , “Triaxial Small-Strain Viscoelastic-ViscoplasticModeling of Asphalt Aggregate Mixes.” Mechanics of Time-Dependent Materials, 2004, Vol8, pp. 365–384.

Malpass, Glen Alan (2003) “The Use of Reclaimed Asphalt Pavement in New Superpave Asphalt Concrete Mixtures.” Doctoral dissertation submitted to the Department of Civil Engineering of North Carolina State University.

Mazzotti, Claudio and Savoia, Marco. “Nonlinear Creep Damage Model for Concrete under Uniaxial Compression.” Journal of Engineering Mechanics., September 2003, pp.1065-1075.

NCHRP Report 547 “Simple Performance Tests: Summary of Recommended Methods and Database”

Roger.D.Corneliussen. “Elastic modulus”. http://www.maropolymeronline.com/Properties/modulus_values.asp 2002.

Rothenburg, L., Bogobowicz, A., Haas, R., Jung, F.W., and Kennepohl, G. (1992). “Micromechanical Modelling of Asphalt Concrete in Connection with Pavement Rutting Problems.” Proceedings of the 7th International Conference on Asphalt Pavements, pp. 230-245.

Saadeh, S., Masad, E., Stuart, K., Abbas, A., Papagainnakis, T., and Al-Khateeb, G. (2003). “Comparative Analysis of Axial and Shear Viscoelastic Properties of Asphalt Mixes.” Journal of the Association of Asphalt Paving Technologists, AAPT, Vol. 72, pp. 122-153.

Sadd, Martin H., Dai, Qingli., Parameswaran, Venkit., and Shukla, Arun., “Microstructural Simulation of Asphalt Materials Modeling and Experimental Verification.” 15th ASCE Engineering Mechanics Conference June 2-5, 2002 Columbia University, New York, NY

Sepehr, K., Svec, O.J., Yue, Z.Q., and El Hussein, H.M. (1994). “Finite Element Modelling of Asphalt Concrete Microstructure.” Computer Aided Assessment and Control of Localized Damage - Proceedings of the International Conference, p 225.

Uddin, W., “A Micromechanical Model For Prediction of Creep Compliance and Viscoelastic Analysis of Asphalt Pavements.” Annual Meeting of Transportation Research Board, November 12 ,1998, Washington D.C

Zhong, Xiaoxiong., Chang, Ching S. “Micromechanical Modeling for Behavior of Cementitious Granular Materials”. Journal of Engineering Mechanics, November, 1999.

Zhu, Han., Chang, Ching S., and Rish, Jeff W., “Normal and tangential compliance for the conforming binder contact I: elastic binder.” International Journal of Solids Structures, Vol 33, No29, pp. 4337-4349, 1996 (a).

Zhu, Han., Chang, Ching S., and Rish, Jeff W., “Normal and tangential compliance for the conforming binder contact II: visco-elastic binder.” International Journal of Solids Structures, Vol 33, No29, pp. 4351-4363, 1996 (b).

VITA

Dong Wang received a Bachelor of Engineering degree in Department of Hydraulic and Hydro-power Engineering from Tsinghua University in Beijing, China in July 2005. In August 2005, he entered the Master program in Civil Engineering of Virginia Polytechnic Institute and State University. He successfully defended his thesis on Aug 2nd, 2007.